Chapter 4

Control of the Flywheel Energy Storage System

In this Chapter the control of the flywheel energy storage system is presented. IDA-PBC controllers for a DFIM and a B2B converter are designed and simulated. Using some extensions of the basic approach, namely simultaneous IDA-PBC (SIDA) and robust IDA-PBC control via structure modification, different controllers for the DFIM are computed and compared. Finally, the whole flywheel energy storage system is simulated with the designed controllers.

Part of the results of this Chapter can also be found in [5][6][8][11][12][13][14].

4.1 Control of a DFIM

Most DFIM controllers proposed in the literature are based on Vector Control and decoupling [54]. This strategy provides a good performance with a simply PI controller through a new coordinate frame. Vector Control (whose basic ideas will be presented later) is widely used for generation systems [90], wind turbines [68][69][85] and energy storage systems [3]. Under the assumption of negligible stator resistances (valid only for large machines) the problem can be formulated as a rotor current control objective. The control scheme reduces to a high gain control rotor current and external loops to achieve the desired goals (mechanical speed or active power, together with the reactive power). Some further developments of vector control for a DFIM with so called sensorless schemes are presented in [44][89].

Some other authors have proposed diferent algorithms for the doubly-fed induction machine. The work of Peresada *et al.* [70][71] is specially relevant. In [70] an indirect stator-flux oriented output feedback controller is presented for mechanical torque tracking objective. Using a similar idea, an output feedback controller for the stator currents is designed in [71], within the stator voltage synchronous reference frame. Other authors propose an state-feedback linearization controller [18] or, using passivity-based techniques, the control design of a DFIM interconnected with an induction machine [17].

In all cases the control of the DFIM is done in a hierarchic way: an inner–loop controls the electrical variables and an outer–loop achieves the mechanical objectives by setting the desired values of the electrical variables. This is based on the fact that the electrical variables are usually much faster than the mechanical ones. Furthermore, in most cases the inner-loop control requires the reconstruction of the magnetic flux variables.

The main contributions of this thesis with respect to previous control schemes of the

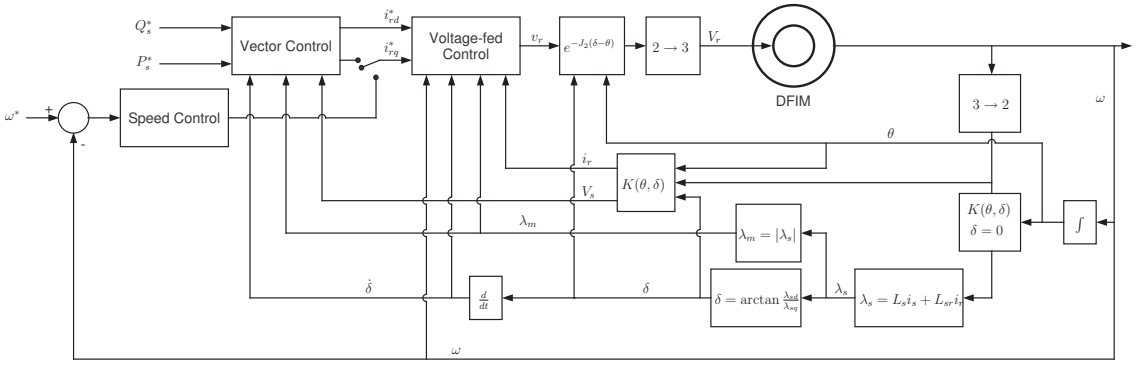

Figure 4.1: Control structure of the Vector Control strategy.

DFIM are twofold: on one hand, a new controller, not requiring flux reconstruction, is designed using standard IDA-PBC techniques; on the other, a global controller for the electric and mechanical parts is constructed by means of the SIDA method. Several modifications, which improve the robustness of the controllers in front parameter variation, are also presented.

4.1.1 Vector Control for a doubly-fed induction machine

Vector Control works by changing coordinates to a frame aligned with any flux variable, either stator, rotor or magnetizing [54]. This new framework allows to decouple, on one hand, the stator reactive power Q_s with one rotor current component, and on the other hand, either the stator active power P_s (generation mode) or the electrical torque τ_e (motor mode). In this section a brief introduction to stator-flux oriented control is presented.

Figure 4.1 shows the control structure of the stator-flux vector control. Two steps are required to design the complete controller. The first block, named "Vector Control", expresses the power (P_s and Q_s) and mechanical (for instance τ_e) inputs in terms of the rotor currents i_r. A second block, "Voltage-fed Control", is used to obtain the desired rotor currents by means of the rotor voltages.

From the two phase model of the DFIM (1.10), new coordinate variables are defined by means of the following transformation:

$$y^r = K(\theta, \delta) y,$$

where $y \in \mathbb{R}^4$ are the $\alpha\beta$ two-phase variables, $y^r \in \mathbb{R}^4$ are the rotated variables and

$$K(\theta, \delta) = \begin{bmatrix} e^{J_2 \delta} & O_2 \\ O_2 & e^{J_2(\delta-\theta)} \end{bmatrix} \in \mathbb{R}^{4\times 4},$$

where δ is an arbitrary function of time[1]. After this transformation the inductance matrix becomes constant

$$\mathcal{L} = \begin{bmatrix} L_s I_2 & L_{sr} I_2 \\ L_{sr} I_2 & L_r I_2 \end{bmatrix} \in \mathbb{R}^{4\times 4},$$

[1]Notice that by selecting the appropriate δ the well-known Blondel-Park transformation is recovered (see subsection 1.2.3).

and

$$\lambda^r = \mathcal{L} i^r. \tag{4.1}$$

From the two-phase equations (1.10), and applying the transformation in fluxes λ, currents i, and voltages v the following electrical equations are obtained

$$\dot{\lambda_s^r} + \dot{\delta} J_2 \lambda_s^r + R_s I_2 i_s^r = V_s^r \tag{4.2}$$

$$\dot{\lambda_r^r} + (\dot{\delta} - \omega) J_2 \lambda_r^r + R_r I_2 i_r^r = V_r^r. \tag{4.3}$$

For stator-flux oriented control the phase δ is selected as

$$\delta = \arctan\left(\frac{\lambda_{s\beta}}{\lambda_{s\alpha}}\right)$$

where $\lambda_{s\alpha}$ and $\lambda_{s\beta}$ are the stator fluxes in $\alpha\beta$ coordinates respectively, which implies

$$\lambda_s^r = e^{J_2\delta}\lambda_{s\alpha\beta} = \begin{bmatrix} \lambda_m \\ 0 \end{bmatrix}$$

where $\lambda_m = |\lambda_s|$. In the steady-state and for balanced systems, the modulus of the flux is a constant. Using this fact and the relation

$$\lambda_r^r = \frac{L_{sr}}{L_s}\lambda_s^r + \sigma i_r^r$$

with $\sigma = L_r - \frac{L_{sr}^2}{L_s}$ obtained from (4.1), equations (4.2) and (4.3) yield

$$\dot{\delta} J_2 \lambda_s^r + R_s I_2 i_s^r = V_s^r$$

$$\sigma \dot{i_r^r} + (\dot{\delta} - \omega) J_2 \left(\frac{L_{sr}}{L_s}\lambda_s^r + \sigma i_r^r\right) + R_r I_2 i_r^r = V_r^r.$$

with $\lambda_s^r = [\lambda_m, 0]^T$,

$$\dot{\delta}\begin{bmatrix} 0 \\ \lambda_m \end{bmatrix} + R_s I_2 i_s^r = V_s^r \tag{4.4}$$

$$\sigma \dot{i_r^r} + (\dot{\delta} - \omega)\frac{L_{sr}}{L_s}\begin{bmatrix} 0 \\ \lambda_m \end{bmatrix} + (\dot{\delta} - \omega)\sigma J_2 i_r^r + R_r I_2 i_r^r = V_r^r. \tag{4.5}$$

To simplify the notation, in the sequel the super–index $(\cdot)^r$ will be omitted.

As explained above, the DFIM can act both in generator mode and in motor mode. Since in both cases Q_s is a control objective, let us derive the relation between the reactive power and the d-rotor current i_{rd}. From definition of reactive power (in a 2-phase system)

$$Q_s = i_s^T J_2 V_s$$

and, using the relation between the currents and fluxes (4.1), $i_s = \frac{1}{L_s}\left(\begin{bmatrix} \lambda_m \\ 0 \end{bmatrix} - L_{sr} i_r\right)$,

$$Q_s = \frac{1}{L_s}\left(\begin{bmatrix} \lambda_m \\ 0 \end{bmatrix} - L_{sr} i_r\right)^T J_2 V_s$$

Notice that if $R_s \sim 0$, using equation 4.4 and having the goal $Q_s = 0$ in mind, a linear relation between the reactive power and the d-component of the rotor current is obtained,

$$i_{rd} = \frac{\lambda_m}{L_{sr}}.$$

For the motor case mode, the relation between the electrical torque τ_e and the q-rotor current component i_{rq} can be computed. Starting with τ_e, definition (1.14), and using the relation between fluxes and currents

$$\tau_e = L_{sr} i_s^T J_2 i_r = \frac{L_{sr}}{L_s} \left(\begin{bmatrix} \lambda_m \\ 0 \end{bmatrix} - L_{sr} i_r^T \right) J_2 i_r = -\frac{L_{sr}}{L_s} \lambda_m i_{rq}. \tag{4.6}$$

For the generator case the interesting relation is the one between the active power P_s and the q-component of the rotor currents. With the active power definition

$$P_s = i_s^T V_s,$$

the stator equation (4.4), and using for i_s the equation derived for the Q_s analysis done before, one obtains

$$P_s = i_s^T \left(-\dot{\delta} \begin{bmatrix} 0 \\ \lambda_m \end{bmatrix} + R_s i_s \right) = -\dot{\delta} \frac{L_{sr}}{L_s} \lambda_m i_{rq} + R_s \frac{1}{L_s^2} (\lambda_m^2 - 2 L_{sr} \lambda_m i_{rd} - L_{sr}^2 |i_r|^2).$$

A typical consideration is that R_s is negligible, and the last relation becomes

$$P_s = -\dot{\delta} \frac{L_{sr}}{L_s} \lambda_m i_{rq}.$$

Voltage-fed control

As shown in Figure 4.1, a inner loop current control is required in order to obtain the rotor voltages to be supplied to the machine. From rotor equations (4.5), a voltage control with a PI contribution can be defined as

$$v_r = (\dot{\delta} - \omega) \frac{L_{sr}}{L_s} \begin{bmatrix} 0 \\ \lambda_m \end{bmatrix} + (\dot{\delta} - \omega) \sigma J_2 i_r + R_r I_2 i_r - K_p (i_r - i_r^*) - K_i \int (i_r - i_r^*) dt, \tag{4.7}$$

where i_r^* are the desired rotor currents obtained in the "Vector Control" block. With this control law the rotor current dynamics becomes

$$\sigma \dot{i_r} = -K_p (i_r - i_r^*) - K_i \int (i_r - i_r^*) dt$$

which is asymptotically stable to i_r^*. Notice that the control law (4.7) has two parts: the first three terms eliminate non-linear parts and decouple the dq-components, while the last two force the convergence to the equilibrium point.

Speed control

The typical output of the vector control method in motor mode is the electrical torque τ_e, while the most common output in applications of the electrical drives is the mechanical speed. This subsection presents an outer loop to achieve speed control of the DFIM. From

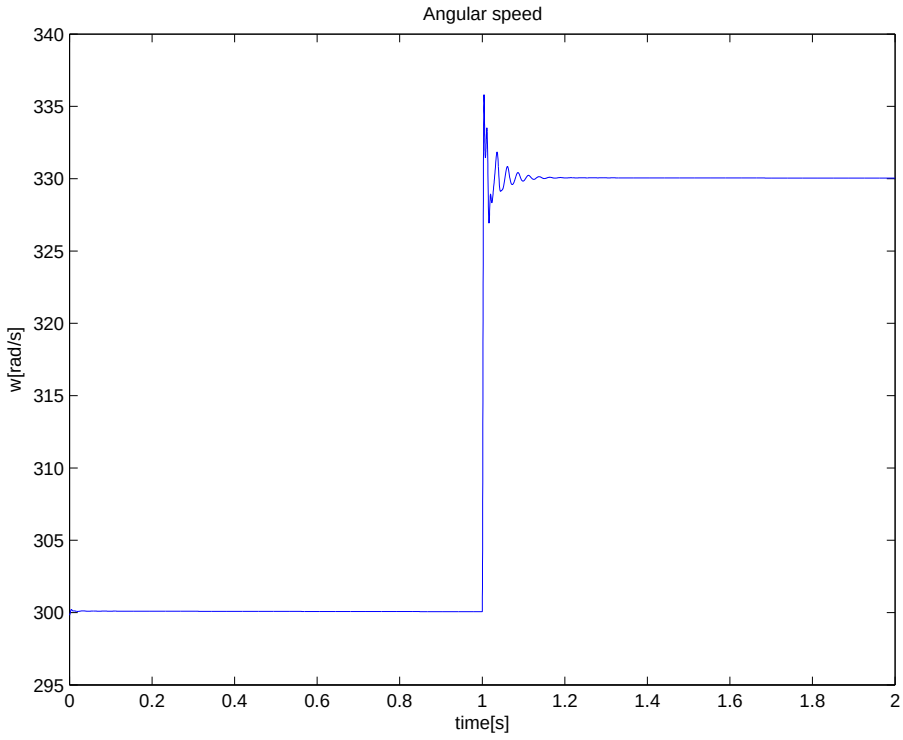

Figure 4.2: Simulation results, Vector Control: angular speed, ω

the mechanical equation (1.15), and using equation (4.6), the following linear dynamical equation is obtained

$$J_m\dot{\omega} = -\frac{L_{sr}}{L_s}\lambda_m i_{rq} - B_r\omega - \tau_L.$$

Using the same kind of arguments than in the previous subsection, the q-rotor current is defined as

$$i_{rq} = -\frac{L_s}{L_{sr}\lambda_m}\left((B_r\omega + \tau_L) + K_{\omega p}(\omega - \omega^*) + K_{\omega i}\int(\omega - \omega^*)dt\right). \tag{4.8}$$

Simulations

The parameter values used in the simulations are (in SI units): $L_{sr} = 0.71$, $L_s = 0.725$, $L_r = 0.715$, $R_s = 4.92$, $Rr = 4.42$, $J_m = 0.00512$, $B_r = 0.005$. The control parameters have been tuned in to $K_p = 5$, $K_{\omega p} = 10$, $K_i = 1$ and $K_{\omega i} = 5$.

We have simulated a step where the desired angular speed ω^* goes from 300rad·s^{-1} to 330rad·s^{-1} at $t = 1$ second. Figure 4.15 shows the angular speed behaviour. The stator voltage and current of one of the phases are displayed in Figure 4.3. Notice that the reactive power is close to zero in any of the steady states. Finally, Figure 4.4 shows the control action in the rotor voltages.

4.1.2 IDA-PBC for a doubly-fed induction machine

Following the classic IDA-PBC method, a controller for a doubly-fed induction machine was designed in [12]. To obtain a globally defined control law a state-dependent damping

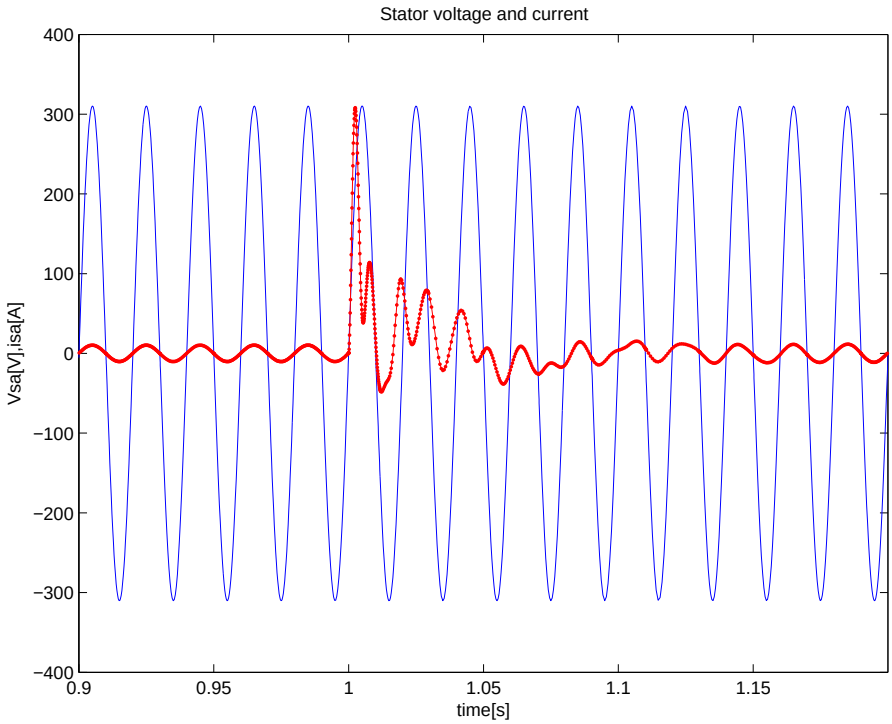

Figure 4.3: Simulation results, Vector Control: stator voltage and current, V_{sa} and i_{sa}

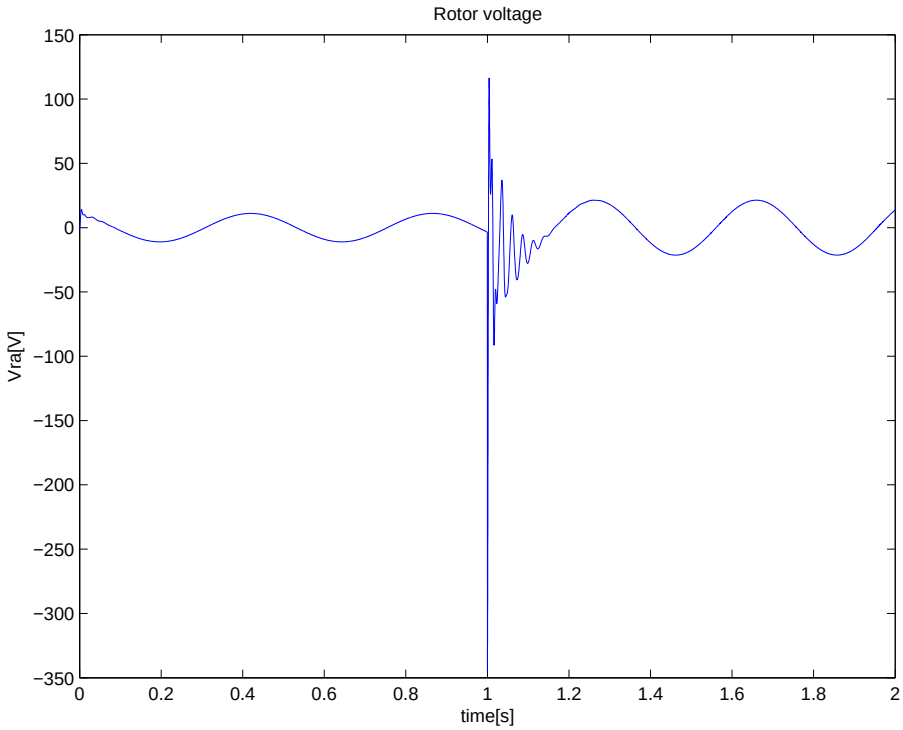

Figure 4.4: Simulation results, Vector Control: rotor voltage, V_{ra}

term is introduced that has the nice interpretation of effectively decoupling the electrical and mechanical parts of the system. This results in a stable controller parameterized by two degrees of freedom.

Let us recall the PCHS model of the DFIM presented in Section 2.5. The Hamiltonian variables are

$$x = [\lambda_s^T, \lambda_r^T, J_m\omega]^T = [x_e^T, x_m]^T$$

where $x_e^T = [\lambda_s^T, \lambda_r^T]$ are the electrical variables, $x_m = J_m\omega$ is the mechanical variable, and the Hamiltonian function is

$$H(x) = \frac{1}{2}x_e^T\mathcal{L}^{-1}x_e + \frac{1}{2J_m}x_m^2$$

$$\mathcal{L} = \begin{bmatrix} L_sI_2 & L_{sr}I_2 \\ L_{sr}I_2 & L_rI_2 \end{bmatrix}.$$

Finally, the interconnection, damping and port matrices are

$$J = \begin{bmatrix} -\omega_sL_sJ_2 & -\omega_sL_{sr}J_2 & O_{2\times1} \\ -\omega_sL_{sr}J_2 & -(\omega_s-\omega_r)L_rJ_2 & L_{sr}J_2i_s \\ O_{1\times2} & L_{sr}i_s^TJ_2 & 0 \end{bmatrix} \quad R = \begin{bmatrix} R_sI_2 & O_{2\times2} & O_{2\times1} \\ O_{2\times2} & R_rI_2 & O_{2\times1} \\ O_{1\times2} & O_{1\times2} & B_r \end{bmatrix}$$

$$g = \begin{bmatrix} I_2 & O_{2\times2} & O_{2\times1} \\ O_{2\times2} & I_2 & O_{2\times1} \\ O_{1\times2} & O_{1\times2} & 1 \end{bmatrix}, \quad u = [v_s^T, v_r^T, \tau_L]^T,$$

while fluxes and currents are related by $i = \partial_\lambda H$, or

$$\begin{bmatrix} \lambda_s \\ \lambda_r \end{bmatrix} = \mathcal{L}\begin{bmatrix} i_s \\ i_r \end{bmatrix}.$$

Fixed points

As mentioned above, the classic IDA-PBC method requires the knowledge of the complete equilibrium point. A fixed point of the DFIM (see Section 1.4, equations (1.17, 1.18, 1.19)) is a solution of the five-dimensional system of equations

$$\begin{aligned} \omega_sL_sJ_2i_s^* + \omega_sL_{sr}J_2i_r^* + R_sI_2i_s^* - v_s &= 0 \qquad (4.9) \\ (\omega_s-\omega^*)[L_{sr}J_2i_s^* + L_rJ_2i_r^*] + R_rI_2i_r^* - v_r^* &= 0 \\ L_{sr}i_s^{*T}J_2i_r^* - B_r\omega^* - \tau_L &= 0. \qquad (4.10) \end{aligned}$$

Notice that the third equation includes a possible external torque τ_L.

Solving the Matching Equation

Following the strategy outlined in subsection 3.3.1, the matching equation (3.8) is equivalent to

$$(J_d(x) - R_d(x))\partial H_a = -(J_a(x) - R_a(x))\partial H + g(x)u. \qquad (4.11)$$

Taking the desired quadratic total energy as

$$H_d(x) = \frac{1}{2}(x_e - x_e^*)^T\mathcal{L}^{-1}(x_e - x_e^*) + \frac{1}{2J_m}(x_m - x_m^*)^2,$$

which clearly has a global minimum at the desired fixed point, yields

$$H_a(x) = H_d(x) - H(x) = -x_e^{*T}\mathcal{L}^{-1}x_e - \frac{1}{J_m}x_m^* x_m + \frac{1}{2}x_e^{*T}\mathcal{L}^{-1}x_e^* + \frac{1}{2J_m}x_m^{*2}.$$

Notice that

$$\partial H_a = \begin{bmatrix} -i^* \\ -\omega^* \end{bmatrix}.$$

Using this relation, (4.11) becomes

$$(J_d(x) - R_d(x)) \begin{bmatrix} i^* \\ \omega^* \end{bmatrix} = [J_a(x) - R_a(x)] \begin{bmatrix} i \\ \omega \end{bmatrix} - gu. \tag{4.12}$$

The control action v_r appears on the third and fourth rows, which suggests the choice

$$J_a(x) = \begin{bmatrix} O_2 & O_2 & O_{2\times 1} \\ O_2 & O_2 & -\mathcal{J}_{rm}(x) \\ O_{1\times 2} & \mathcal{J}_{rm}^T(x) & 0 \end{bmatrix}, \quad R_a = \begin{bmatrix} O_2 & O_2 & O_{2\times 1} \\ O_2 & rI_2 & O_{2\times 1} \\ O_{1\times 2} & O_{1\times 2} & 0 \end{bmatrix} \tag{4.13}$$

where $\mathcal{J}_{rm}(x) \in \mathbb{R}^{2\times 1}$ is to be determined. An additional resistor $r > 0$ for the rotor currents has been included in order to damp the transient oscillations.

Substituting (4.13) in (4.12) and using the fixed-point equations, one gets, after some algebra,

$$\begin{aligned} \mathcal{J}_{rm}^T(x) &= L_{sr}\frac{(i_r - i_r^*)^T}{|i_r - i_r^*|^2}(i_s - i_s^*)^T J_2 i_r^*, \\ v_r &= v_r^* - (\omega - \omega^*)(L_r J_2 i_r^* + \mathcal{J}_{rm}(x)) - L_{sr}\omega^* J_2(i_s - i_s^*) - rI_2(i_r - i_r^*). \end{aligned}$$

Unfortunately, the control is singular at the fixed point. Although from a numerical point of view this problem can be solved by introducing a regularization parameter, it is actually possible to get rid of the singularity by adding a variable damping which turns out to decouple the mechanical and electrical subsystems.

Subsystem Decoupling via State–Dependent Damping

Now we take $H_d(x)$ and $J_d(x)$ as before, but instead of the constant R_a given in (4.13) a state–dependent damping matrix is introduced

$$R_a(x) = \begin{bmatrix} O_2 & O_2 & O_{2\times 1} \\ O_2 & rI_2 & O_{2\times 1} \\ O_{1\times 2} & O_{1\times 2} & \xi(x) \end{bmatrix},$$

where

$$\xi(x) = \frac{\tau_e^* - \tau_e(x_e)}{\omega - \omega^*} \tag{4.14}$$

with τ_e the electrical torque

$$\tau_e = L_{sr} i_s^T J_2 i_r$$

and $\tau_e^* = B_r\omega^*$ its fixed point value. Notice that, when substituted into the closed-loop Hamiltonian equations, $\xi(x)$ is multiplied by $\omega - \omega^*$ and hence no singularity is introduced.

Since only the mechanical part of (4.12) is changed, only the value for $\mathcal{J}_{rm}(x)$ is altered, while the expression for v_r in terms of $\mathcal{J}_{rm}(x)$ remains the same. After some algebra and using the fixed point equations, one gets

$$\mathcal{J}_{rm}(x) = L_{sr} J_2 i_s.$$

The closed loop dynamical system is still of the form (3.4) with

$$J_d(x) = \begin{bmatrix} -\omega_s L_s J_2 & -\omega_s L_{sr} J_2 & O_{2\times 1} \\ -\omega_s L_{sr} J_2 & -(\omega_s - \omega) L_r J_2 & O_{2\times 1} \\ O_{1\times 2} & O_{1\times 2} & 0 \end{bmatrix}, R_d(x) = \begin{bmatrix} R_s I_2 & O_2 & O_{2\times 1} \\ O_2 & (R_r + r) I_2 & O_{2\times 1} \\ O_{1\times 2} & O_{1\times 2} & B_r + \xi(x) \end{bmatrix}.$$

Notice that the state–dependent "damping" is an artifice to decouple the electrical and mechanical parts in the closed-loop interconnection and dissipation matrices—and the proposed control is shaping only the electrical dynamics. From (4.14) it follows that the sign of $B_r + \xi(x)$ is indefinite, and depends on the state space point and, in particular on the way a given trajectory approaches the fixed point.

Main Stability Result

Due to the fact that is not possible to use $B_r + \xi(x) \geq 0$, the standard stability analysis for PCH systems (see Proposition 1 of Section 2.1 and [87]) cannot be applied. However, the overall system has a nice cascaded structure, with the electrical part a *bona fide* PCH subsystem with well–defined dissipation. (This situation is similar to the Nested PBC proposed in Chapter 8 of [63].) Asymptotic stability of the overall system follows from well known properties of cascaded systems [83]. For the sake of completeness we present the specific result required for our system in the following lemma.

Lemma 4.1. *Let us consider a system of the form*

$$\begin{aligned} \dot{x_1} &= f_1(x_1, x_2), \\ \dot{x_2} &= -B x_2 + h(x_1), \end{aligned} \tag{4.15}$$

where $x_1 \in \mathbb{R}^n$, $x_2 \in \mathbb{R}$, $B > 0$ and h is a continuous function. Assume that the system has fixed points x_1^*, x_2^*, and $\lim_{t\to+\infty} x_1(t) = x_1^*$ for any $x_2(t)$. Then $\lim_{t\to+\infty} x_2(t) = x_2^*$.

Proof. Let $(\sigma_1(t), \sigma_2(t))$ be a given solution to (4.15). Since $\lim_{t\to+\infty} \sigma_1(t) = x_1^*$ it follows that $\sigma_1(t)$ is bounded and so is $h(\sigma_1(t))$. Since $B x_2^* = h(x_1^*)$, it follows that $\forall \epsilon > 0$ there exists $T > 0$, which may depend on $\sigma_1(t)$ and $\sigma_2(t)$, such that if $t > T$ then $|h(\sigma_1(t)) - B x_2^*| < \epsilon \frac{B}{2}$. Using

$$1 = e^{-Bt} + B \int_0^t e^{-B(t-\tau)} \mathrm{d}\tau$$

it is immediate to write,

$$\begin{aligned} \sigma_2(t) - x_2^* &= e^{-Bt}(x_2(0) - x_2^*) + \int_0^t e^{-B(t-\tau)}(h(\sigma_1(\tau)) - B x_2^*)\mathrm{d}\tau \\ &= e^{-Bt}(x_2(0) - x_2^*) + \int_0^T e^{-B(t-\tau)}(h(\sigma_1(\tau)) - B x_2^*)\mathrm{d}\tau \\ &+ \int_T^t e^{-B(t-\tau)}(h(\sigma_1(\tau)) - B x_2^*)\mathrm{d}\tau \end{aligned}$$

where $t > T$ has been assumed. There exists $\tilde{T} > 0$ such that if $t > \tilde{T}$ then

$$e^{-Bt}\left(x_2(0) - x_2^* + \int_0^T e^{B\tau}(h(\sigma_1(\tau)) - Bx_2^*)\mathrm{d}\tau\right) < \frac{\epsilon}{2},$$

where the boundedness of h has been used. Furthermore

$$\left|\int_T^t e^{-B(t-\tau)}(h(\sigma_1(\tau)) - Bx_2^*)\mathrm{d}\tau\right| < \int_T^t e^{-B(t-\tau)}\epsilon\frac{B}{2}\mathrm{d}\tau = \frac{\epsilon}{2}(1 - e^{-B(t-T)}) < \frac{\epsilon}{2}.$$

Finally, taking $t > \max\{T, \tilde{T}\}$, one gets $|\sigma_2(t) - x_2^*| < \epsilon$. This ends the proof. □

The results obtained in this subsection can be summarized in the following proposition.

Proposition 4.2. *Consider the DFIM PCHS–based system described in Section 2.5 in closed–loop with the static state–feedback control*

$$v_r = v_r^* - (\omega - \omega^*)(L_r J_2 i_r^* + L_{sr} J_2 i_s) - L_{sr}\omega^* J_2(i_s - i_s^*) - rI_2(i_r - i_r^*), \tag{4.16}$$

where

$$v_r^* = (\omega_s - \omega^*)[L_{sr} J_2 i_s^* + L_r J_2 i_r^*] + R_r I_2 i_r^*.$$

and (i_s^*, i_r^*, ω^*) correspond to desired equilibria. Assume the motor friction coefficient B_r is sufficiently small to ensure the solution of the equilibrium equations. Then the system is globally convergent.

Proof. Energy shaping of the electrical subsystem ensures that

$$\dot{H}_{de} \leq -\min\{R_s, R_r + r\}|x_e - x_e^*|^2,$$

where $H_{de} \triangleq \frac{1}{2}(x_e - x_e^*)^T\mathcal{L}^{-1}(x_e - x_e^*)$. Consequently, $x_e \to x_e^*$ exponentially fast. The proof follows immediately checking that the conditions of Lemma 1. To do that, we identify x_1 with the electric variables and x_2 with the mechanical variable. The electric subsystem has (i_s^*, i_r^*) as a global asymptotically stable fixed point for any function $\omega(t)$. Hence, all trajectories of the closed–loop dynamics asymptotically converge to the equilibrium point (i_s^*, i_r^*, ω^*). □

Simulations

Numerical simulations have been run to validate the designed controller. The simulation parameters are (in SI units): $L_s = 0.725$,$L_r = 0.715$, $L_{sr} = 0.71$, $R_r = 4.42$, $R_s = 4.95$, $J_m = 0.001$, $B_r = 0.005$, $\tau_L = -3.7$, $v_s = [310.27, 0]^T$ and $\omega_s = 2\pi 50$. The controller parameter is selected as $r = 100$.

The numerical experiment is performed using the DFIM as a *motor*. The DFIM starts at $\omega = 314\text{rad}\cdot\text{s}^{-1}$ and the desired speed is set at $\omega^* = \omega^d = 350\text{rad}\cdot\text{s}^{-1}$ for $t \geq 0.5\text{s}$. To improve the power factor, we have set the second (q) component of i_s^* to zero.

Figures 4.5 and 4.6 shows the behaviour of the mechanical speed ω and the stator currents, i_s. Notice that the control objectives are achieved and the systems stabilizes at the desired fixed point. Figure 4.7 shows the phase portrait of the mechanical speed and the stator currents, which shows that the electrical subsystem is much faster than the mechanical one. This is also depicted in Figure 4.8, where it can be seen that the

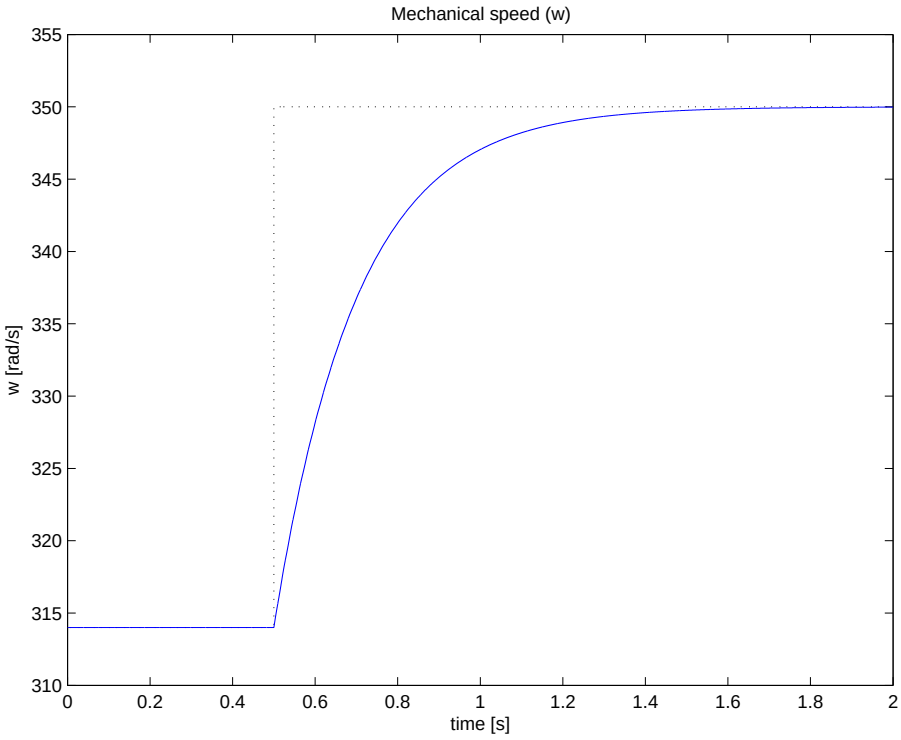

Figure 4.5: Simulation results, IDA-PBC: Mechanical speed, ω.

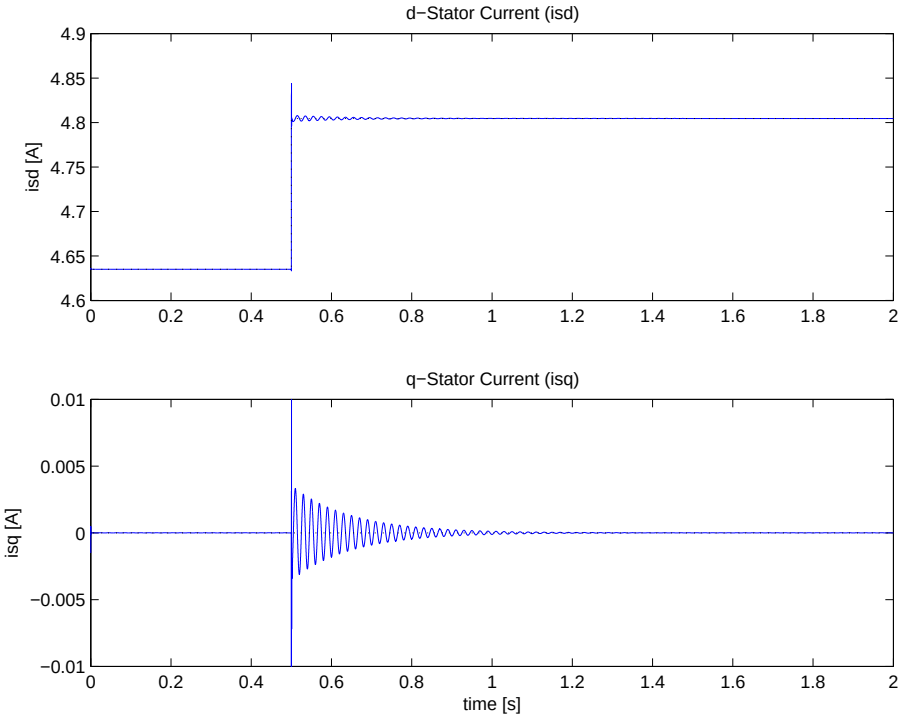

Figure 4.6: Simulation results, IDA-PBC: Stator currents, i_s.

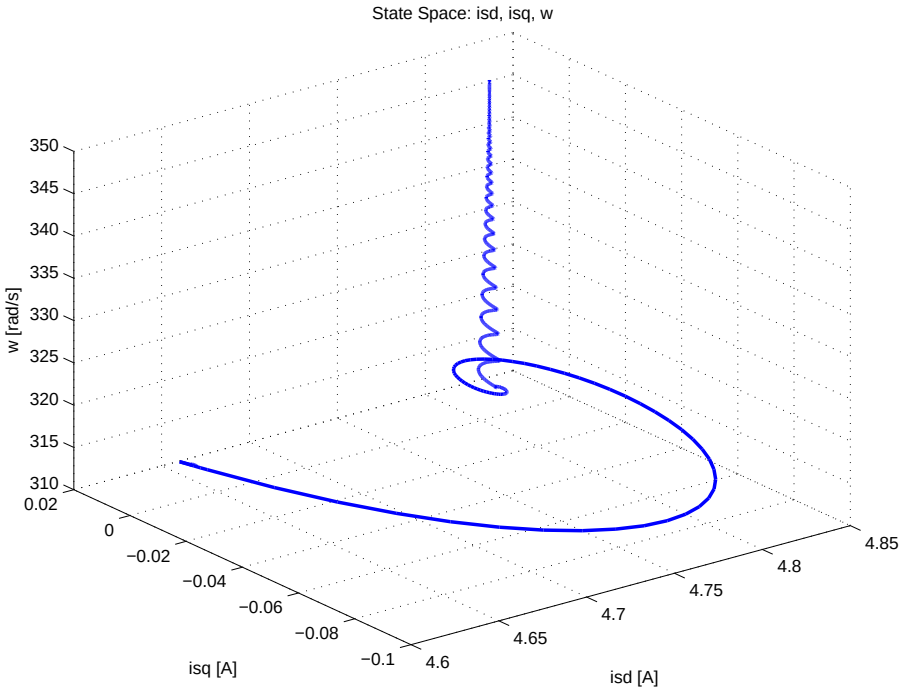

Figure 4.7: Simulation results, IDA-PBC: Phase portrait, i_s and ω.

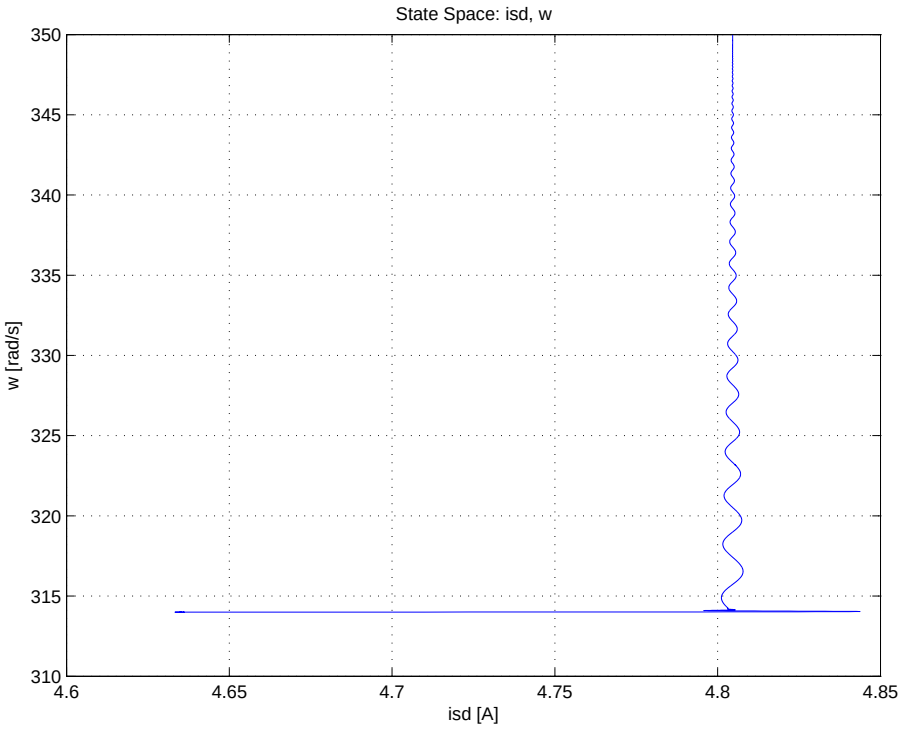

Figure 4.8: Simulation results, IDA-PBC: Phase portrait, i_{sd} and ω.

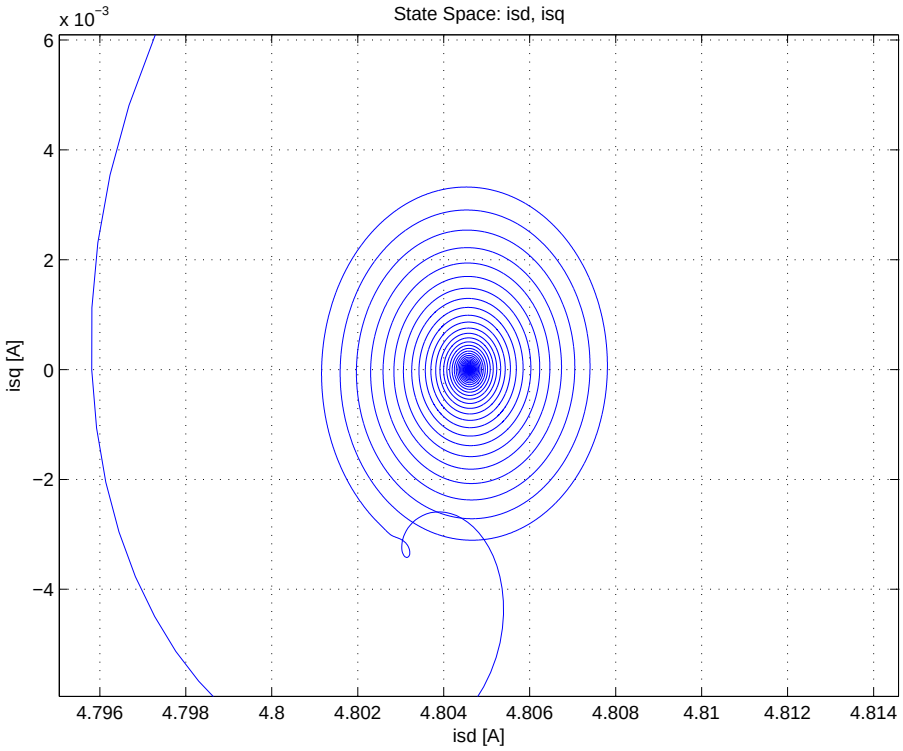

Figure 4.9: Simulation results, IDA-PBC: Detail of the phase portrait, i_{sd} and i_{sq}.

dynamics is already close to the fixed point for the components of the stator currents while the mechanical speed is still on its transient. This slow response of the mechanical variable is associated to the cascaded structure of the controller and will be improved in the next subsection using the SIDA variant of IDA-PBC. Finally, Figure 4.9 shows the state space of the stator currents.

4.1.3 Simultaneous IDA-PBC for a DFIM

In the previous subsection the equilibria is stabilized with IDA–PBC that shape the electrical energy, treating the mechanical dynamics as a cascaded subsystem.

The nested–loop architecture, with an inner–loop to control the electrical subsystem and an outer–loop (usually a simple PI) to control the mechanical variables, is prevalent in classical electromechanical systems applications, where it is justified invoking time–scale separation arguments. Intrinsic to the nested–loop configuration is the fact that the time response of the mechanical subsystem is subordinated to the electrical transient. This may lead to below–par performances in small stand–alone DFIM–based generating units where a fast response of the mechanical speed is needed to ensure efficient control of the power flow and, furthermore, the mechanical and electrical time constants may be close. The purpose of this Section is to show that using SIDA–PBC it is possible to shape the energy function of the *complete* system dynamics, resulting in a controller with improved power–flow regulation performance. To the best of our knowledge, this is the first control algorithm for this class of systems that provides for this additional degree of freedom.

SIDA–PBC Design

The desired energy function is fixed as

$$H_d(x) = \frac{1}{2}\tilde{x}^T P \tilde{x}, \quad P = P^T > 0, \tag{4.17}$$

where we defined $\tilde{(\cdot)}$ as the error, $\tilde{(\cdot)} = (\cdot) - (\cdot)^*$. The SIDA–PBC design boils down to finding a matrix $F_d(x)$ solution of

$$[J(i_s, \omega) - R]\partial H + \begin{bmatrix} v_s \\ O_{2\times 1} \\ \tau_L \end{bmatrix} + \begin{bmatrix} O_{2\times 2} \\ I_2 \\ O_{1\times 2} \end{bmatrix} v_r = F_d(x) P \tilde{x}, \tag{4.18}$$

and verifying $F_d(x) + F_d^T(x) \leq 0$. To simplify the solution we restrict P to be diagonal and—for reasons that will become clear below—set the first row, third column entry of $F_d(x)$ to zero, that is,

$$P = \begin{bmatrix} p_s I_2 & O_{2\times 2} & O_{2\times 1} \\ O_{2\times 2} & p_r I_2 & O_{2\times 1} \\ O_{1\times 2} & O_{1\times 2} & p_\omega \end{bmatrix} > 0, \quad F_d(x) = \begin{bmatrix} F_{11}(x) & F_{12}(x) & O_{2\times 1} \\ F_{21}(x) & F_{22}(x) & F_{23}(x) \\ F_{31}^T(x) & F_{32}^T(x) & F_{33}(x) \end{bmatrix},$$

where the partition of $F_d(x)$ is conformal with the partition of P.

From the first two rows of (4.18), after using the relationship between fluxes and currents (4.1) and the equilibria equation (4.9), one obtains

$$-(\omega_s L_s J_2 + R_s I_2)\tilde{i}_s - \omega_s L_{sr} J_2 \tilde{i}_r = (L_s F_{11} p_s + L_{sr} F_{12} p_r)\tilde{i}_s + (L_{sr} F_{11} p_s + L_r F_{12} p_r)\tilde{i}_r,$$

which, for all $\tilde{i}_s, \tilde{i}_r$, has a unique solution given by

$$\begin{aligned} F_{11} &= -\frac{1}{p_s}\left(\omega_s J_2 + \frac{L_r}{\mu} R_s I_2\right) \\ F_{12} &= \frac{L_{sr}}{p_r \mu} R_s I_2 \end{aligned}$$

where $\mu \triangleq L_s L_r - L_{sr}^2 > 0$.

We remark that this simple calculation was possible because the 13–element of $F_d(x)$ was set to zero. The price paid for having this term equal to zero is that it makes the selection of $F_{31}(x)$ critical. Indeed, this term will appear in the corners of $F_d(x) + F_d^T(x)$, that we recall should be *negative semi–definite*. The term $F_{32}(x)$, on the other hand, is not critical because its contribution to $F_d(x) + F_d^T(x)$ can be countered by a suitable selection of $F_{23}(x)$ that, in view of the presence of the control, is totally free. These issues will become clearer as we go through the calculations below.

From the fifth row of (4.18) and (4.1) we get

$$\begin{aligned} \begin{bmatrix} F_{31}^T(x) p_s & F_{32}^T(x) p_r \end{bmatrix} \mathcal{L}\tilde{i} + F_{33}(x) p_\omega J_m \tilde{\omega} &= L_{sr} i_s^T J_2 i_r - B_r \omega \\ &= L_{sr} \begin{bmatrix} -i_r^{*T} J_2 & i_s^T J_2 \end{bmatrix} \tilde{i} - B_r \tilde{\omega} \end{aligned}$$

with the second identity obtained adding and substracting the equilibrium equation (4.10). From the $\tilde{\omega}$ term we get

$$F_{33} = -\frac{B_r}{p_\omega J_m},$$

while the remaining equations can be arranged as

$$\tilde{i}^T \left(L \begin{bmatrix} p_s F_{31}(x) \\ p_r F_{32}(x) \end{bmatrix} - L_{sr} \begin{bmatrix} J_2 i_r^* \\ -J_2 i_s \end{bmatrix} \right) = 0, \tag{4.19}$$

where we have defined

$$L \triangleq \begin{bmatrix} L_s I_2 & L_{sr} I_2 \\ L_{sr} I_2 & L_r I_2 \end{bmatrix}.$$

Although a solution for $F_{31}(x)$ and $F_{32}(x)$ of this equation can be easily obtained—inverting L to set the term inside the parenthesis equal to zero—it turns out that we do not have enough flexibility in the control to generate a matrix $F_d(x)$ that satisfies the skew–symmetry constraint of J_d, and we have to look for an alternative solution. Towards this end, notice that we can add to (4.19) any vector $G(x) \in \mathbb{R}^4$

$$\tilde{i}^T \left(L \begin{bmatrix} p_s F_{31}(x) \\ p_r F_{32}(x) \end{bmatrix} - L_{sr} \begin{bmatrix} J_2 i_r^* \\ -J_2 i_s \end{bmatrix} - G(x) \right) = 0 \tag{4.20}$$

as long as

$$\tilde{i}^T G(x) = 0.$$

Setting the term inside the parenthesis of (4.20) equal to zero we get

$$\begin{bmatrix} p_s F_{31}(x) \\ p_r F_{32}(x) \end{bmatrix} = \frac{L_{sr}}{\mu} \begin{bmatrix} L_r J_2 i_r^* + L_{sr} J_2 i_s \\ -L_r J_2 i_s - L_{sr} J_2 i_r^* \end{bmatrix} + \begin{bmatrix} G_C(x) \\ G_D(x) \end{bmatrix}, \tag{4.21}$$

where, for convenience, we have introduced the partition

$$\begin{bmatrix} G_C(x) \\ G_D(x) \end{bmatrix} = L^{-1} G(x)$$

with $G_C(x), G_D(x) \in \mathbb{R}^2$. As indicated above, to satisfy the skew–symmetry condition it is necessary to generate a solution with $F_{31}(x)$ *constant*. This is easily achieved selecting

$$G_C(x) = -\frac{L_{sr}^2}{\mu} J_2 \tilde{i}_s. \tag{4.22}$$

With this selection $G(x)$ results in

$$G(x) = \begin{bmatrix} -\frac{L_{sr}^2 L_r}{\mu} J_2 \tilde{i}_s + L_{sr} G_D \\ -\frac{L_{sr}^3}{\mu} J_2 \tilde{i}_s + L_r G_D \end{bmatrix}$$

and, in order to ensure $\tilde{i}^T G(x) = 0$, we fix

$$G_D(x) = -\frac{L_{sr}^2}{\mu} J_2 \tilde{i}_r \tag{4.23}$$

Finally, replacing (4.22) and (4.23) in (4.21) we get

$$\begin{aligned} F_{31} &= \frac{L_{sr}}{p_s \mu} J_2 (L_{sr} i_s^* + L_r i_r^*) = \frac{L_{sr}}{p_s \mu} J_2 \lambda_r^* \\ F_{32}(x) &= -\frac{L_{sr}}{p_r \mu} J_2 (L_s i_s + L_{sr} i_r) = -\frac{L_{sr}}{p_r \mu} J_2 \lambda_s. \end{aligned}$$

The next step is to select the remaining terms of $F_d(x)$—that are directly affected by the control action—to satisfy the skew–symmetry constraint of J_d. To simplify the condition, we select

$$F_{21} = -F_{12}, \quad F_{23}(x) = -F_{32}(x), \quad F_{22} = -\frac{k_r}{2p_r} I_2 < 0$$

which yields

$$F_d(x) + F_d^T(x) = \begin{bmatrix} -\frac{2L_r R_s}{p_s \mu} I_2 & O_{2\times 2} & \frac{L_{sr}}{p_s \mu} J_2 \lambda_r^* \\ O_{2\times 2} & -\frac{k_r}{p_r} I_2 & O_{2\times 1} \\ -\frac{L_{sr}}{p_s \mu} \lambda_r^{*T} J_2 & O_{1\times 2} & -\frac{2B_r}{p_\omega J_m} \end{bmatrix}.$$

A simple Schur's complement analysis establishes that $F_d(x) + F_d^T(x) < 0$ if and only if the *free parameters* p_s and p_ω satisfy

$$p_s > \left(\frac{J_m L_{sr}^2}{4 B_r L_r R_s \mu} |\lambda_r^*|^2 \right) p_\omega. \tag{4.24}$$

Remark 4.3. The inequality (4.24) clearly reveals the critical role played by B_r. If this parameter is small $\frac{p_s}{p_\omega}$ has to be large. In the next Section we compute the control law and we see that this can be achieved injecting a high gain in the current loop or reducing the gain on the speed error feedback—both options inducing obvious detrimental effects on the closed-loop performance. △

Proposed Controller and Stability Analysis

Once we have solved the SIDA–PBC matching equations, the design is completed computing the controller and assessing its stability properties. This is summarized in the proposition below.

Proposition 4.4. *Consider the DFIM PCHS–based system described in Section 2.5 in closed–loop with the static feedback control*

$$v_r = R_r i_r + (\omega_s - \omega) J_2 (L_{sr} i_s + L_r i_r) - k_s (L_s \tilde{i}_s + L_{sr} \tilde{i}_r) - k_r (L_{sr} \tilde{i}_s + L_r \tilde{i}_r) + k_\omega J_2 \lambda_s \tilde{\omega} \tag{4.25}$$

where $k_r > 0$, $k_\omega > 0$ and

$$k_s > \frac{L_{sr}^2}{4 B_r L_r \mu} |\lambda_r^*|^2 k_\omega.$$

The closed–loop system is then described by $\dot{x} = F_d(x) \partial H_d$, with $H_d(x)$ defined in (4.17), and $F_d(x) + F_d^T(x) < 0$. Consequently, the equilibrium x^* is globally exponentially stable.

Proof. From the second row of (4.18) we obtain

$$v_r = R_r i_r + (\omega_s - \omega) J_2 (L_{sr} i_s + L_r i_r) + F_{21} p_s \tilde{\lambda}_s + F_{22} p_r \tilde{\lambda}_r + F_{23}(z) p_\omega J_m \tilde{\omega}.$$

The control law (4.25) follows from this expression after substitution of the values of F_{ij}, using (4.1) and defining

$$k_s \triangleq \frac{p_s L_{sr} R_s}{p_r \mu}, \quad k_\omega \triangleq \frac{p_\omega J_m L_{sr}}{p_r \mu}.$$

Finally, the lower bound on $\frac{k_s}{k_\omega}$ is obtained from the inequality (4.24). □

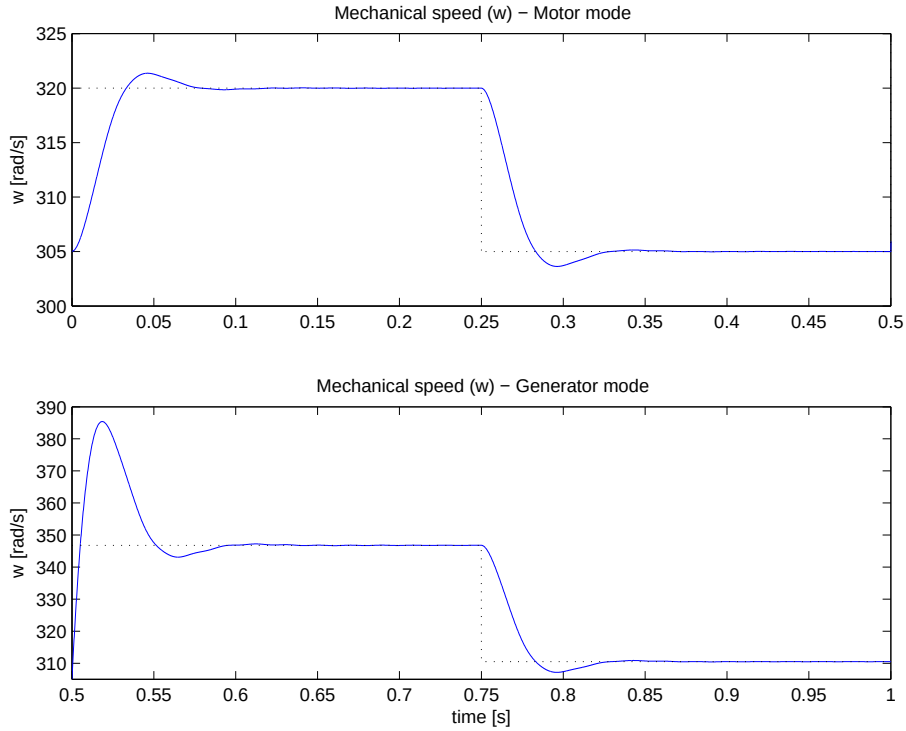

Figure 4.10: Simulation results, SIDA-PBC: Mechanical speed, ω.

Simulations

The simulation parameters are (in SI units): $L_s = L_r = 0.011$, $L_{sr} = 0.01$, $R_r = R_s = 0.01$, $J_m = 0.001$, $B_r = 0.005$, $v_s = [310.27, 0]^T$ and $\omega_s = 2\pi 50$. The controller parameters are selected as $k_s = 1000$, $k_r = 100$ and $k_\omega = 0.01$.

The first numerical experiment is performed using the DFIM as a *motor* (for $0 < t \leq 0.5$s). In this case $\tau_L = -5$N·m and the desired speed is $\omega^* = \omega^d = 320\text{rad}\cdot\text{s}^{-1}$ for $0 < t \leq 0.25$s and $\omega^* = \omega^d = 305\text{rad}\cdot\text{s}^{-1}$ for $0.25\text{s} < t \leq 0.5$s. The second simulation is done using the DFIM as a generator (for $0.5\text{s} < t \leq 1$s). In this case $\tau_L = 5$N·m and the desired current is $i_s^* = i_s^d = [-2.7, 0]^T$A for $0.5\text{s} < t \leq 0.75$s and $i_s^* = i_s^d = [-2.85, 0]^T$A for $0.75\text{s} < t \leq 1$s. Notice that, to improve the power factor, we have set the second (q) component of i_s^* to zero. The behavior of the mechanical speed and the d and q–components of the stator current for both simulations are depicted in Figs. 4.10, 4.11 and 4.12, respectively.

In Figure 4.13 we compare the speed behaviour of the new SIDA-PBC with the IDA–PBC reported in [12]—that shapes only the electrical energy. The simulation conditions are the same as before but, in view of the slower response of the controller of subsection 4.1.2 (see also [12]), we had to scale up the time. As expected, in spite of the large damping coefficient used in the IDA–PBC ($r = 1000$), SIDA–PBC achieves a much faster speed response.

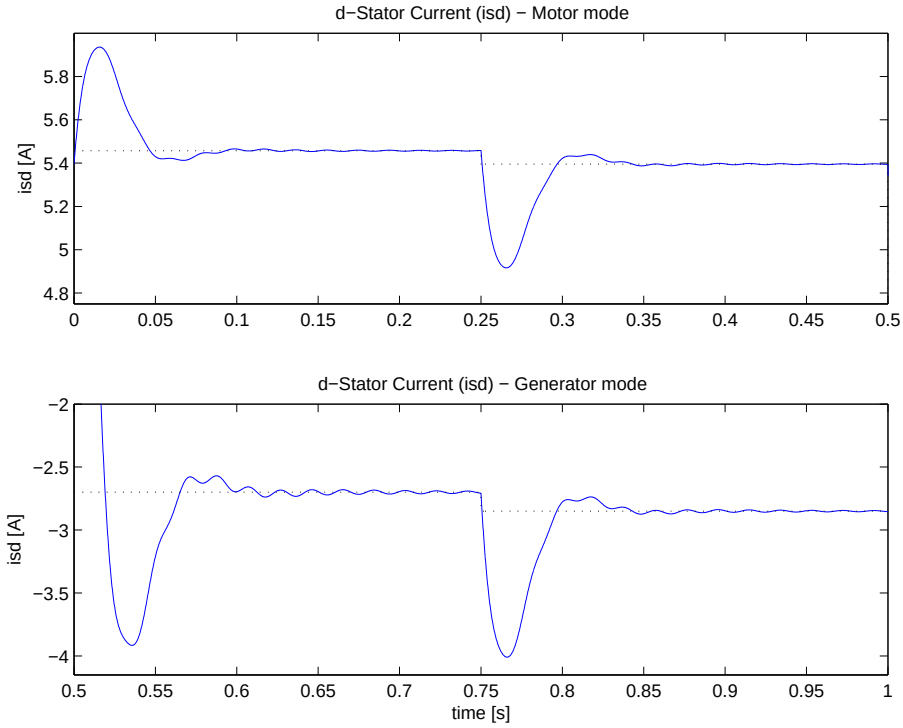

Figure 4.11: Simulation results, SIDA-PBC: Stator current d-component.

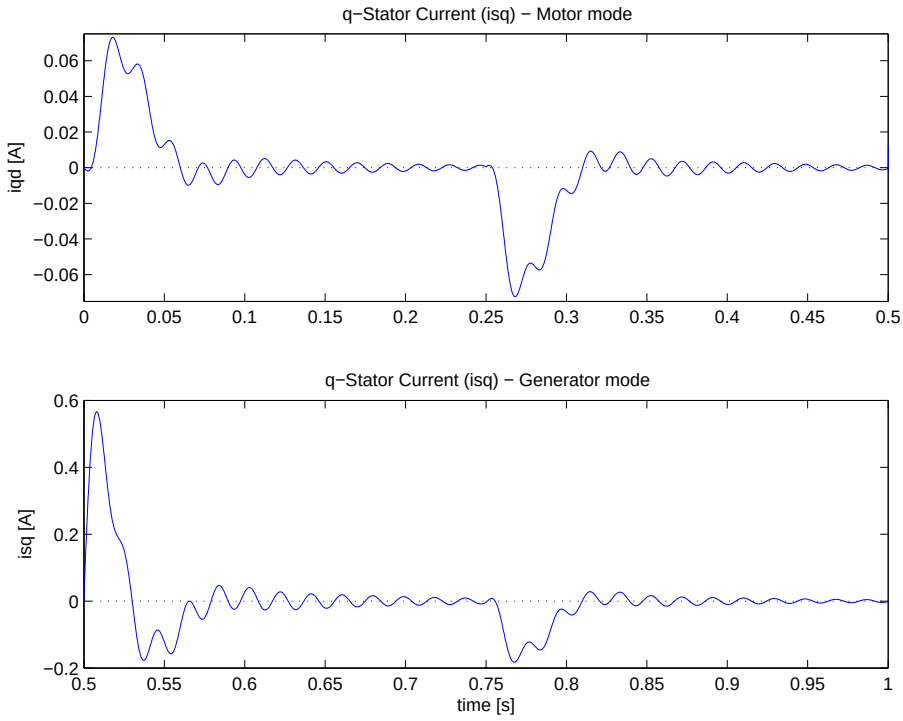

Figure 4.12: Simulation results, SIDA-PBC: Stator current q-component.

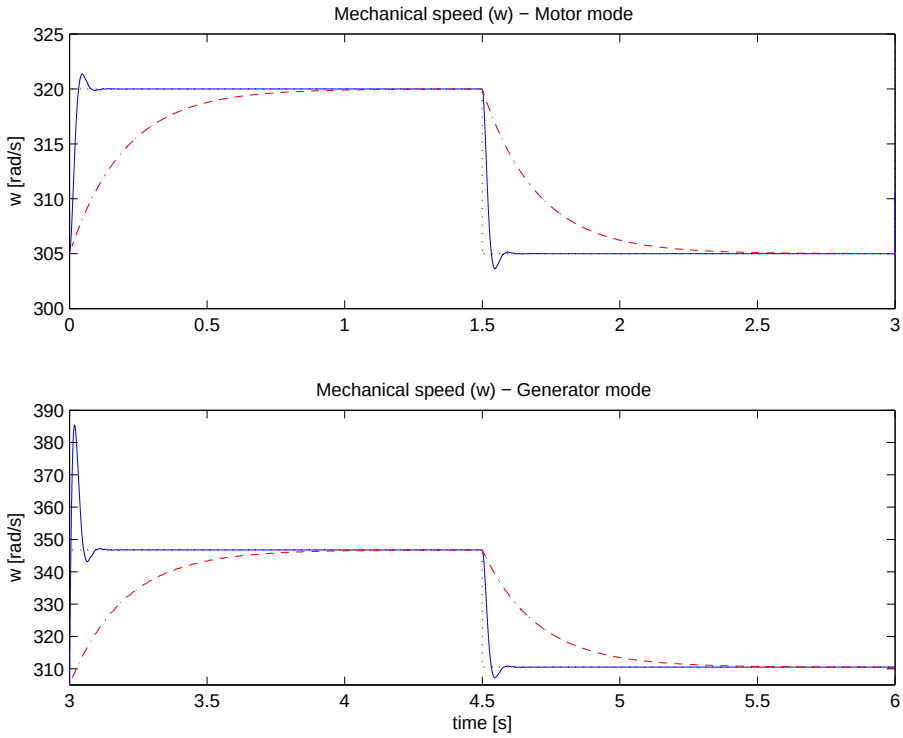

Figure 4.13: Simulation results: Mechanical speed, ω, for SIDA–PBC (continuous line) and IDA–PBC (dashed line).

4.1.4 Robust controller for a DFIM

As mentioned in Section 3.4, the main problem when implementing an IDA-PBC (or SIDA) controller is the robustness. In subsection 3.4.3 a new procedure to avoid (or to minimize) the parameter dependence of the final controller is presented. Following those ideas, a new control law is designed here for the electrical part of the DFIM. The main advantage respect to the controller designed in subsection 4.1.2 is that the fixed point is only a function of the stator currents and no error is added through the fixed point computation.

The obtained controller is more robust respect to the previous ones based on IDA-PBC. Even so, in order to implement it on the experimental plant, two new modifications are introduced, outside of the IDA-PBC framework. On one hand, an outer-loop speed control is designed (in the same spirit of the Vector Control, subsection 4.1.1) to improve the transient behavior of the mechanical speed. Furthermore, an integral term is added in the inner (or current) loop to increase robustness in front external perturbations.

Figure 4.14 shows the scheme of the complete control algorithm. It includes all the required dq-transformations to show the simplicity of the proposed controller in front of the Vector Control strategy, Figure 4.1. The main advantages are:

- The stator flux λ_s is not required to compute λ_m. This dispenses with the estimation of a critical variable which will be used to construct the rotating reference.
- The rotating reference is referred to the stator voltage v_s which, as discussed in the previous item, is easier to obtain than the stator flux orientated reference. In other

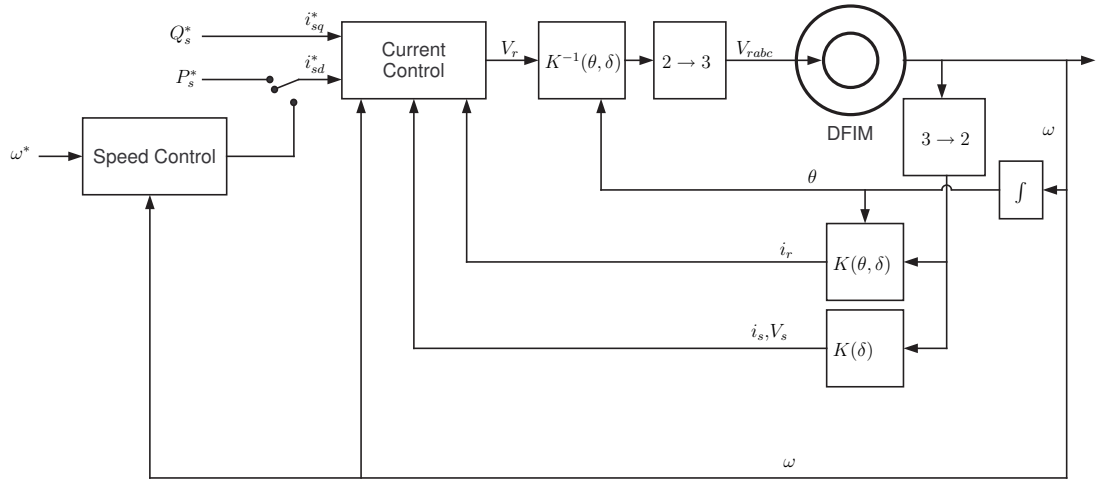

Figure 4.14: Control structure of the IDA-PBC based proposed controller.

words, computations depend only on a measured variable.

- The reference inputs of the new controller are directly the stator currents (which are the outputs of the electrical subsystem), whereas the reference inputs of the inner-loop of the Vector Control are the rotor currents.

- No assumption is made on the smallness of R_s.

The design control is organized as follows. First the new IDA-PBC approach is used to obtain an stator current control. Next, using linear control theory an integral term is added. Finally, the outer-loop speed control is designed.

Robust IDA-PBC controller for a DFIM

In this subsection we present a more robust IDA-PBC controller for the electrical part of the DFIM. This new controller improves the previous one (subsection 4.1.2) in that the proportional action is directly applied to the desired output, i_s. The design procedure is based on the so-called robust IDA-PBC controller via structure modification methodology, presented in subsection 3.4.3.

Consider the electrical subsystem of the DFIM, written in the stator reference frame,

$$\dot{\lambda} = \begin{bmatrix} -\omega_s L_s J_2 - R_s I_2 & -\omega_s L_{sr} J_2 \\ -(\omega_s - \omega) L_{sr} J_2 & -(\omega_s - \omega) L_r J_2 - R_r I_2 \end{bmatrix} i + \begin{bmatrix} v_s \\ v_r \end{bmatrix} \tag{4.26}$$

where $\lambda = \mathcal{L} i$ and $\mathcal{L} = \mathcal{L}^T > 0$. This system can be expressed in current terms as $(x = i)$

$$\mathcal{L}\dot{x} = \begin{bmatrix} f_o(x) \\ f_u(x) + g(x)u \end{bmatrix}$$

where the control input is $u = v_r$, and

$$f_o(x) = -(\omega_s L_s J_2 + R_s I_2) i_s - \omega_s L_{sr} J_2 i_r + v_s \tag{4.27}$$

$$f_u(x) = -(\omega_s - \omega) L_{sr} J_2 i_s - ((\omega_s - \omega) L_r J_2 + R_r I_2) i_r \tag{4.28}$$

$$g(x) = I_2 \tag{4.29}$$

Consider now the following target dynamics

$$\mathcal{L}\dot{x} = (J_d - R_d)\partial H_d.$$

This system has a PCHS form with new coordinates $z = \mathcal{L}x$ and the stability is guaranteed provided that $J_d = -J_d^T$, $R_d = R_d^T \geq 0$ and $x^* = \arg\min H_d(x)$. This desired Hamiltonian function differs from the original one in the $\mathcal{L}$ matrix, but, as $\mathcal{L} = \mathcal{L}^T > 0$, it only affects the transient while the stability properties are kept. Then we can apply the methodology of proposition 17 (in subsection 3.4.3).

First we fix $\partial_o H_d$ (where the x_o variables are the stator currents i_s) as

$$\partial_o H_d = i_s - i_s^d$$

which ensures stability of the i_s^d fixed point. Then, from (3.33),

$$f_o = A(x)\partial_o H_d + B(x_u),$$

where x_u are the rotor currents i_r,

$$-(\omega_s L_s J_2 + R_s I_2)(i_s - i_s^d) - \omega_s L_{sr} J_2 (i_r - i_r^*) = A(x)(i_s - i_s^d) + B(i_r)$$

and $A(x)$ and $B(i_r)$ are

$$A(x) = -(\omega_s L_s J_2 + R_s I_2),$$
$$B(i_r) = -\omega_s L_{sr} J_2 (i_r - i_r^*).$$

Note that condition (3.36), $A + A^T = -2R_s I_2 < 0$, is satisfied. Now we set

$$J_{duo} = -kJ_2 \tag{4.30}$$

which ensures condition (3.37),

$$\left(-(J_{duo}^T)^{-1} B(x_u)\right)\Big|_{i_r = i_r^*} = \left(\frac{1}{k}\omega_s L_{sr}(i_r - i_r^*) I_2\right)\Big|_{i_r = i_r^*} = 0$$

and condition (3.38)

$$\partial_u \left(-(J_{duo}^T)^{-1} B(x_u)\right)\Big|_{i_r = i_r^*} = \frac{1}{k}\omega_s L_{sr} I_2 > 0.$$

Finally, the controller obtained from (3.30), $v_r = u = g^{-1}[J_{duo}\partial_o H_d - f_u]$, using (4.27), (4.28), (4.29) and (4.30), is

$$u = (\omega_s - \omega) L_{sr} J_2 i_s + ((\omega_s - \omega) L_r J_2 + R_r I_2) i_r - kJ_2(i_s - i_s^d). \tag{4.31}$$

Let us recover the desired closed-loop Hamiltonian system. From equation (3.31),

$$f_o = (J_{doo} - R_{doo})\partial_o H_d - J_{duo}^T \partial_u H_d$$

with (4.27), (4.28) and (4.30) one gets

$$-(\omega_s L_s J_2 + R_s I_2)(i_s - i_s^d) - \omega_s L_{sr} J_2 (i_r - i_r^*) = (J_{doo} - R_{doo})(i_s - i_s^d) - k J_2 \partial_u H_d$$

which implies

$$J_{doo} - R_{doo} = -(\omega_s L_s J_2 + R_s I_2),$$

and

$$\partial_u H_d = \frac{1}{k} \omega_s L_{sr} (i_r - i_r^*).$$

Notice that the proposed method (see subsection 3.4.3) takes $J_{duu} - R_{duu} = 0$ and $R_{duo} = 0$, so the closed-loop dynamics has the following form

$$\mathcal{L}\dot{x} = \begin{bmatrix} -(\omega_s L_s J_2 + R_s I_2) & -k J_2 \\ -k J_2 & O_2 \end{bmatrix} \partial H_d$$

with the Hamiltonian function

$$H_d(x) = \frac{1}{2}(i_s - i_s^d)^T (i_s - i_s^d) + \frac{1}{2k} \omega_s L_{sr} (i_r - i_r^*)^T (i_r - i_r^*)$$

or, in a compact form, defining $\tilde{(\cdot)}$ as the error, $\tilde{(\cdot)} = (\cdot) - (\cdot)^*$.,

$$H_d(x) = \frac{1}{2} \tilde{x}^T P \tilde{x}$$

where

$$P = \begin{bmatrix} I_2 & O_2 \\ O_2 & \frac{1}{k} \omega_s L_{sr} I_2 \end{bmatrix}.$$

We can also describe this system with Hamiltonian variables $\lambda = \mathcal{L}x$

$$\dot{\lambda} = \begin{bmatrix} -(\omega_s L_s J_2 + R_s I_2) & -k J_2 \\ -k J_2 & O_2 \end{bmatrix} \partial H_{\lambda d},$$

with the Hamiltonian function

$$H_{\lambda d} = \frac{1}{2} \tilde{\lambda}^T P_\lambda \tilde{\lambda},$$

where

$$P_\lambda = (\mathcal{L}^{-1})^T P \mathcal{L}^{-1} = \frac{1}{\mu^2 k} \begin{bmatrix} (L_r^2 k + L_{sr}^3 \omega_s) I_2 & -L_{sr}(L_r k + \omega_s L_s L_{sr}) I_2 \\ -L_{sr}(L_r k + \omega_s L_s L_{sr}) I_2 & L_{sr}(L_{sr} k + L_s^2 \omega_s) I_2 \end{bmatrix}.$$

Adding an integral term

Adding an integral term is required to assure some robustness properties in front of rotor parameters variations (as, for instance, the resistor variations with temperature) or external perturbations. The new control law, v_{ri}, has the form

$$v_{ri} = v_r + k_i J_2 \int \tilde{i}_s dt \tag{4.32}$$

where v_r is the controller obtained in the previous Section, and $k_i > 0$ is the integral control gain. Stability proof (including the integral term) is presented in [14]. Notice that

the controller is, in fact, a feedback linearization term and a PI controller. In contrast to standard practice, the PI is defined with a J_2 skew-symmetric matrix.

To carry out the stability analysis, we find it convenient to express the closed–loop system in an alternative form. Replacing (4.31) with (4.32) in (4.26), and using the definition of equilibria, we can write the closed–loop system in error coordinates as

$$\dot{\tilde{\lambda}}_s = -(\omega_s L_s J_2 + R_s I_2)\tilde{i}_s - \omega_s L_{sr} J_2 \tilde{i}_r \tag{4.33}$$

$$\dot{\tilde{\lambda}}_r = -k J_2 \tilde{i}_s + k_i J_2 \int \tilde{i}_s dt. \tag{4.34}$$

Now, using the relation between fluxes and currents, $\lambda = \mathcal{L} i$ (see subsection 1.2.3),

$$\tilde{i}_r = \frac{1}{L_r}(\tilde{\lambda}_r - L_{sr}\tilde{i}_s)$$

we get

$$\begin{aligned} \dot{\tilde{\lambda}}_s &= L_s \dot{\tilde{i}}_s + L_{sr}\dot{\tilde{i}}_r \\ &= L_s \dot{\tilde{i}}_s + \frac{L_{sr}}{L_r}(\dot{\tilde{\lambda}}_r - L_{sr}\dot{\tilde{i}}_s). \end{aligned}$$

Replacing the last two equations in (4.33), differentiating and using (4.34) we can write the electrical dynamics in the equivalent form

$$D(p)\tilde{i}_s = 0, \tag{4.35}$$

with the polynomial matrix, in the derivative operator $p = \frac{d}{dt}$,

$$D(p) = p^3 I_2 + (c_1 I_2 + c_2 J_2)p^2 + (c_3 I_2 + c_4 J_2)p + c_5 I_2,$$

and the parameters

$$c_1 = \frac{R_s L_r}{\mu}, \quad c_2 = \omega_s - \frac{L_{sr}}{\mu}k, \quad c_3 = \frac{\omega_s L_{sr}}{\mu}k, \quad c_4 = -\frac{L_{sr}}{\mu}k_i, \quad c_5 = \frac{\omega_s L_{sr}}{\mu}k_i.$$

Equation (4.35) describes a linear system of order six whose stability is determined by the characteristic polynomial $\det D(s)$, with $s \in \mathbb{C}$ the Laplace transform variable. Although the study of this (sixth–order) polynomial can be carried out with classical tools, e.g., Routh–Hurwitz criterion, this procedure yields complex parameter relations that complicate the choice of the PI gains. These results are contained in the following proposition, whose proof is given in [14].

Proposition 4.5. *Consider the electrical part of the DFIM system described in Section 2.5, (4.26), in closed–loop with the control (4.32).*

P1. If $k_i = 0$, for all $k > 0$, the electrical coordinates converge to their desired values, while the speed is bounded and also converges to a constant value.

P2. There exists $k_i^M > 0$ such that, for all $k_i \in (0, k_i^M]$ and all $k > 0$, the electrical coordinates converge to their desired values, while the speed is bounded and also converges to a constant value.

Outer-loop speed control

As explained in the previous sections, the i_{sq} value corresponds to the reactive power of the stator side of the machine, so the i_{sq}^* value is assigned according to the desired power factor of the DFIM, while i_{sd} can be used to control the active power (delivered or consumed) by the machine. In a drive application i_{sd}^* is selected so that the target speed is reached. In order to increase the performance and the robustness, an outer-loop speed controller with a PI part is designed. Consider that the current controller is stable, then the mechanical dynamics (see subsection 1.2.3)

$$J_m\dot{\omega} = L_{sr} i_s^T J_2 i_r - B_r\omega - \tau_L$$

can be stabilized by means of

$$i_{sd}^* = \frac{1}{L_{sr} i_{rq}^*}\left(L_{sr} i_{sq}^* i_{rd}^* - B_r\omega^* - \tau_L + k_{\omega p}(\omega - \omega^*) + k_{\omega i}\int(\omega - \omega^*)\mathrm{d}t\right) \tag{4.36}$$

yielding the closed–loop behaviour

$$J\dot{\omega} = -B_r(\omega - \omega^*) - k_{\omega p}(\omega - \omega^*) - k_{\omega i}\int(\omega - \omega^*)\mathrm{d}t.$$

Notice that in a practical implementation this controller could be simplified to a simple PI controller by combining the system dissipation with the proportional part.

Simulations

Numerical simulations are run to validate the controller. The DFIM parameter values are (in SI units): $L_{sr} = 0.01$, $L_r = L_s = 0.011$, $R_s = 0.01$, $R_r = 0.01$, $J_m = 0.001$, $B_r = 0.005$, $\tau_L = -1$, $v_s = [310.27, 0]^T$ and $\omega_s = 2\pi 50$. In the control law the parameters are changed in order to verify the robustness, and the gain parameters are fixed as $k = 1$, $k_i = 1$, $k_{\omega p} = 0.05$ and $k_{\omega i} = 0.02$.

The simulation starts with a desired mechanical speed $\omega^* = 320\text{rad}\cdot\text{s}^{-1}$, and at $t = 1\text{s}$ the desired value is changed to $\omega^* = 350\text{rad}\cdot\text{s}^{-1}$; again, at $t = 2\text{s}$ the external torque changes to $\tau_L = -1.3\text{N}\cdot\text{m}$. In both cases the desired q-stator current is fixed at $i_{sq}^* = 0$ to obtain a good power factor in the stator side.

Figure 4.15 shows the behavior of the mechanical speed. The transient can be tuned by means of the control gain of (4.36) and the integral term drives the mechanical speed to the desired value even, in the presence of the external perturbation (at $t = 2\text{s}$). Figures 4.16 and 4.17 show the behaviour of the stator currents. It can be seen that the electrical subsystem is indeed faster than the mechanical one, and the hypothesis toked account in the outer–loop design Section is true. Notice that the reference of i_{sd} is varying according to the regulation speed and also due to the integral action of the outer control-loop.

4.1.5 Comparison of the controllers. Simulations

This subsection is a summary of the whole section, with the pros and cons of the proposed control laws as deduced from the simulations. Obviously, this kind of comparison is not intended as a contest to select the best overall controller, but it can help to clarify the differences between them.

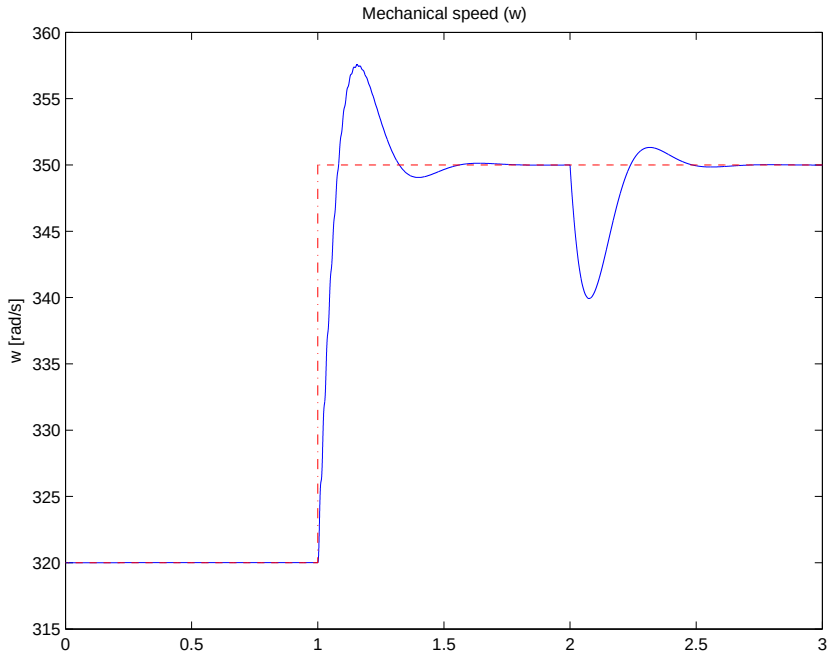

Figure 4.15: Simulation results, Robust Controller: Angular speed under uncertain parameters.

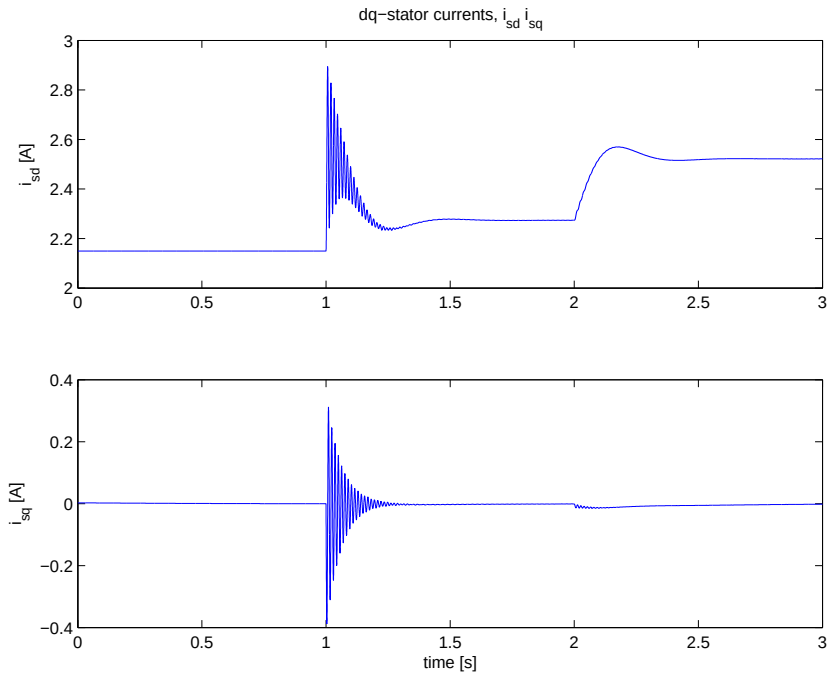

Figure 4.16: Simulation results, Robust Controller: dq-stator currents, i_{sd}, i_{sq},under uncertain parameters.

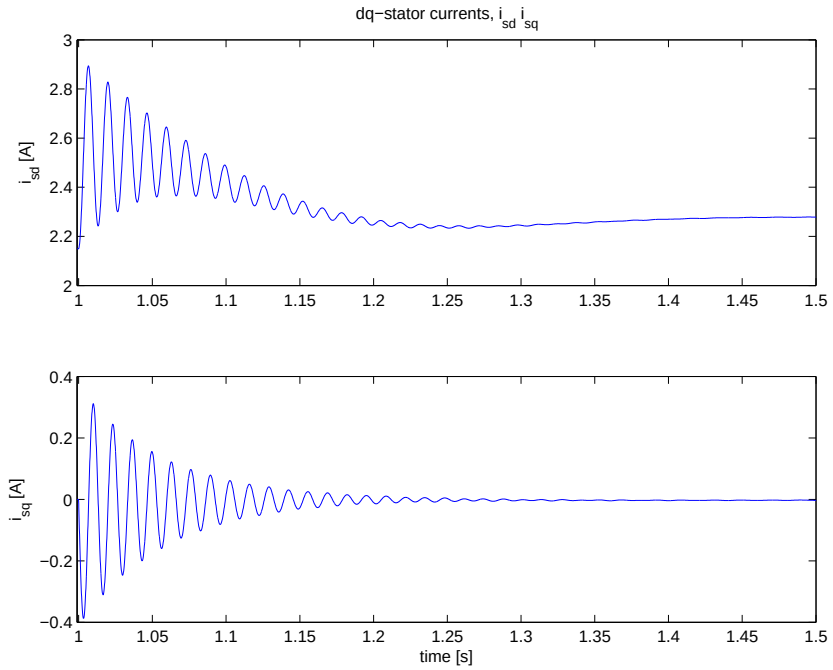

Figure 4.17: Simulation results, Robust Controller: Detail of the dq-stator currents transient.

Let us comment the simulation results. The DFIM parameters are (in SI units): $L_{sr} = 0.71$, $L_s = 0.725$, $L_r = 0.715$, $R_s = 4.92$, $R_r = 4.42$, $J_m = 0.00512$, $B_r = 0.005$ and $\tau_L = \pm 3.7$[2] and the grid parameters are $v_s = [310.27, 0]^T$ and $\omega_s = 2\pi 50$. The control parameters are summarized in Table 4.1.

Algorithm	**Control Parameters**
Vector Control, (4.7, 4.8)	$K_p = 5$, $K_i = 15$, $K_{\omega p} = 10$, $K_{\omega i} = 1$
IDA-PBC, (4.16)	$r = 100$
SIDA-PBC, (4.25)	$k_s = 50$, $k_r = 50$, $k_\omega = 5$
Robust IDA-PBC, (4.31,4.32,4.36)	$k = 10$, $k_i = 1$, $k_{\omega p} = 4$, $k_{\omega i} = 100$

Table 4.1: Simulation parameter values of the proposed controllers for the DFIM.

Simulations are split in two parts: a motor and a generator mode. The motor mode starts for $t = 0$s at $\omega(0) = 305\text{rad}\cdot\text{s}^{-1}$, with a desired speed $\omega^d = 320\text{rad}\cdot\text{s}^{-1}$, and at $t = 1.5$s the target mechanical speed is reduced to to $\omega^d = 305\text{rad}\cdot\text{s}^{-1}$. For the generator mode a similar scenario is simulated. Coming from the last state of the motor mode, at $t = 3$s, the desired active power supplied from the DFIM is set to $P_s^d = -750$W, and at $t = 4.5$s the active power is changed to $P_s^d = -650$W. In both cases the desired reactive power is zero, *i.e.* the stator voltages and currents must be in phase (or in opposite phase).

[2]The sign of τ_L depends on the mode; it is positive for the motor mode and negative for the generator one, *i.e.* it acts as a load or as a drive, respectively.

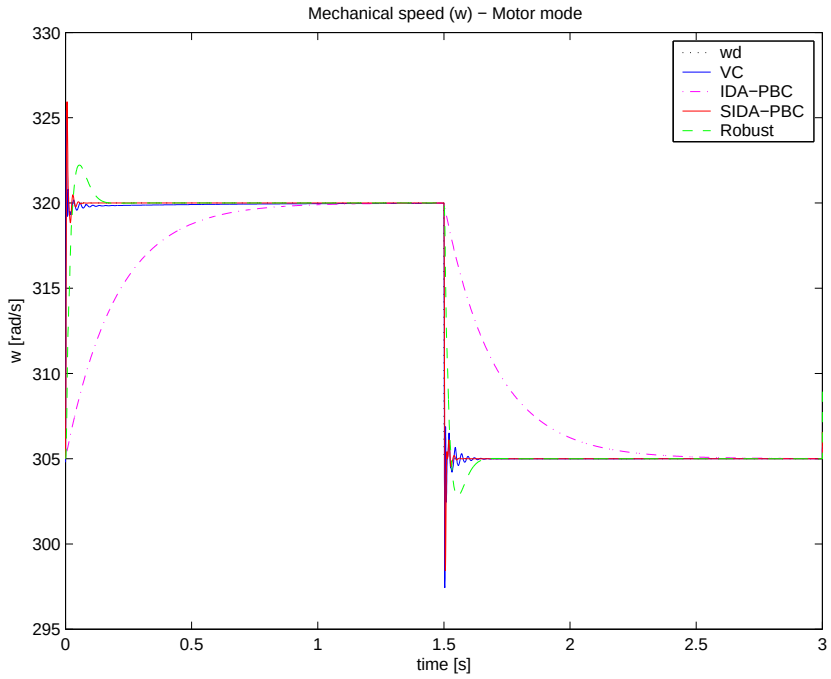

Figure 4.18: Simulation results, comparison: mechanical speed ω for a motor mode.

Figures from 4.18 to 4.23 show the behaviour of the DFIM with different controllers. When the DFIM acts as a motor, the controlled outputs are the mechanical speed ω (Figures 4.18 and 4.19) and the power factor (Figure 4.20). In both cases all the proposed controllers achieve the goals but the transient is slower for the IDA-PBC controller (clearly associated to the *cascaded* control structure).

For the generator mode, the controlled outputs are the active power delivered by the DFIM P_s (Figures 4.21 and 4.22), and also the power factor (Figure 4.23). The worst behavior corresponds to the Vector Control technique. Notice that this is the unique methodology which does not use the stator current i_s as feedback (the power objectives are expressed, with some assumptions, in terms of rotor currents). The power factor objective is achieved for all the controllers.

As mentioned above, the main problem of the implementation of IDA-based controllers is the robustness. To illustrate this drawback, the simulations of Figures 4.24 to 4.26 show the behaviour (in a motor mode) of the proposed controllers under a variation of the 10% of the values of dissipation parameters which enter into computation of the controller ($R_s = 4.428\Omega$, $R_r = 3.978\Omega$ and $B_r = 0.0045\text{N}\cdot\text{m}\cdot\text{rad}^{-1}\text{s}^{-1}$).

Clearly the worst controller under uncertain parameters is the classic IDA-PBC. It is surprising the good behavior of the SIDA-PBC controller, for which, even without an integral term to correct the error, the steady state is close to the desired fixed point. Finally, both the Vector Control and our *robust* controller achieve the mechanical regulation.

Summing up, we have the following:

- **Vector Control**
  - *Pros*: Robustness and fast transient response.

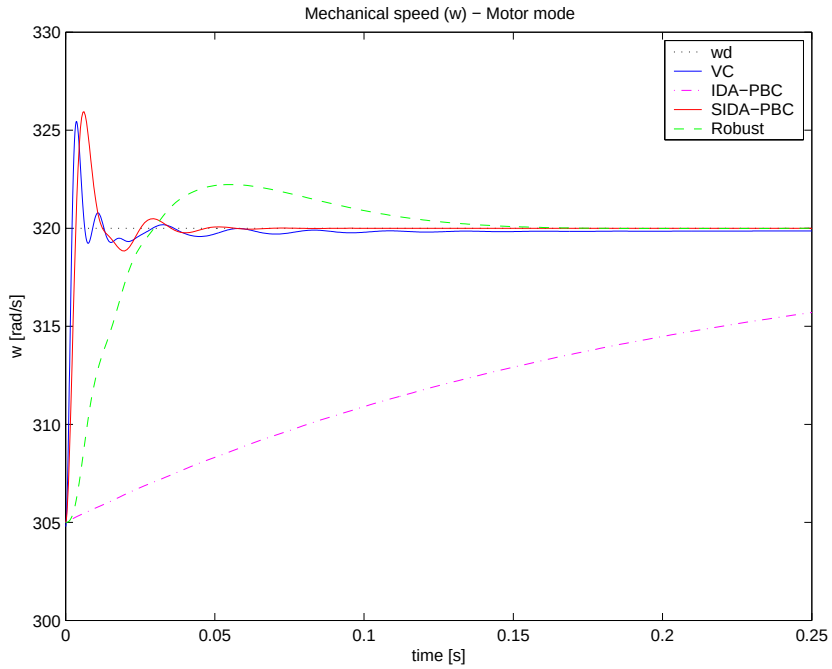

Figure 4.19: Simulation results, comparison: detail of the mechanical speed ω for a motor mode.

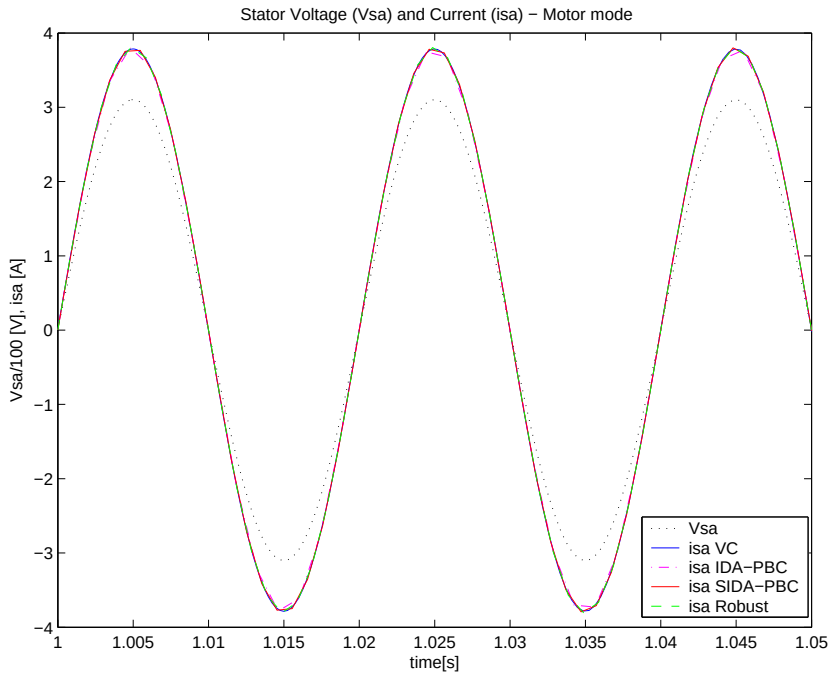

Figure 4.20: Simulation results, comparison: A-stator voltage and current (V_{sa}, i_{sa}) during a motor mode.

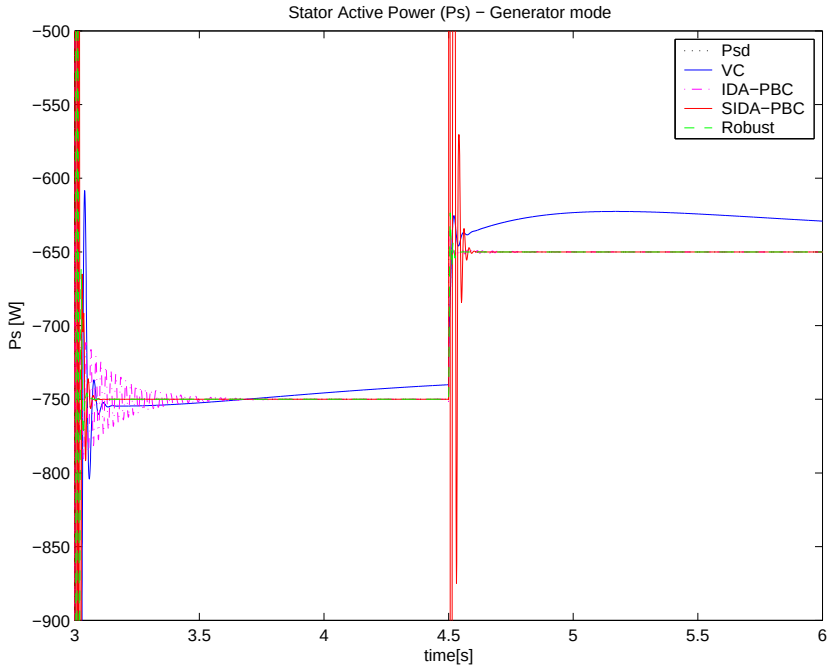

Figure 4.21: Simulation results, comparison: active power P_s for a generator mode.

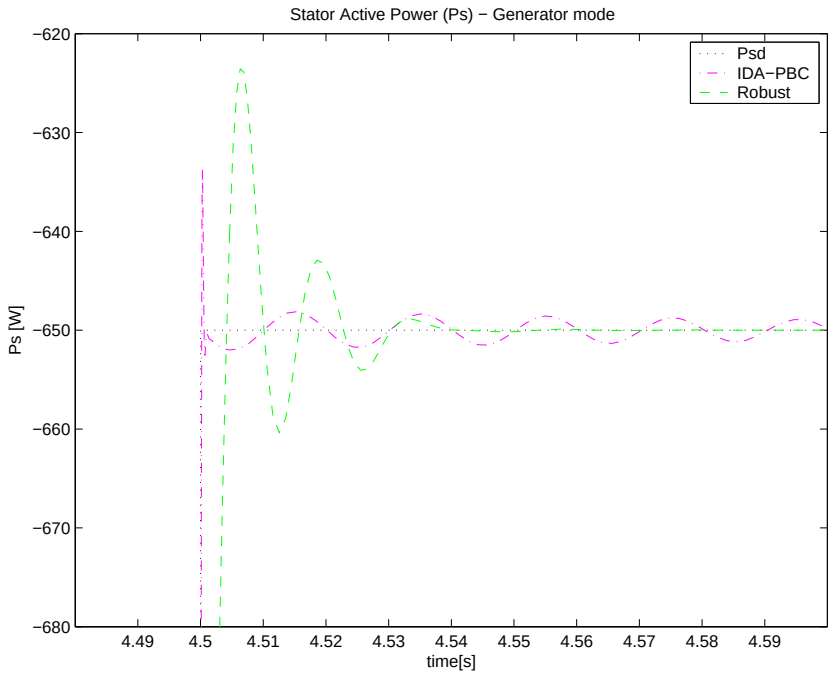

Figure 4.22: Simulation results, comparison: detail of the active power P_s for a generator mode.

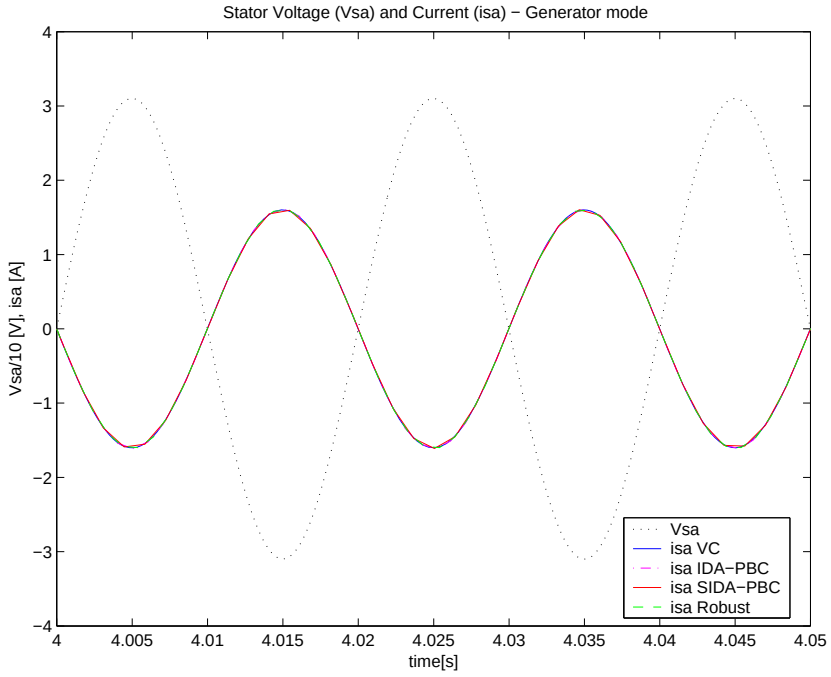

Figure 4.23: Simulation results, comparison: A-stator voltage and current (V_{sa}, i_{sa}) during a generator mode.

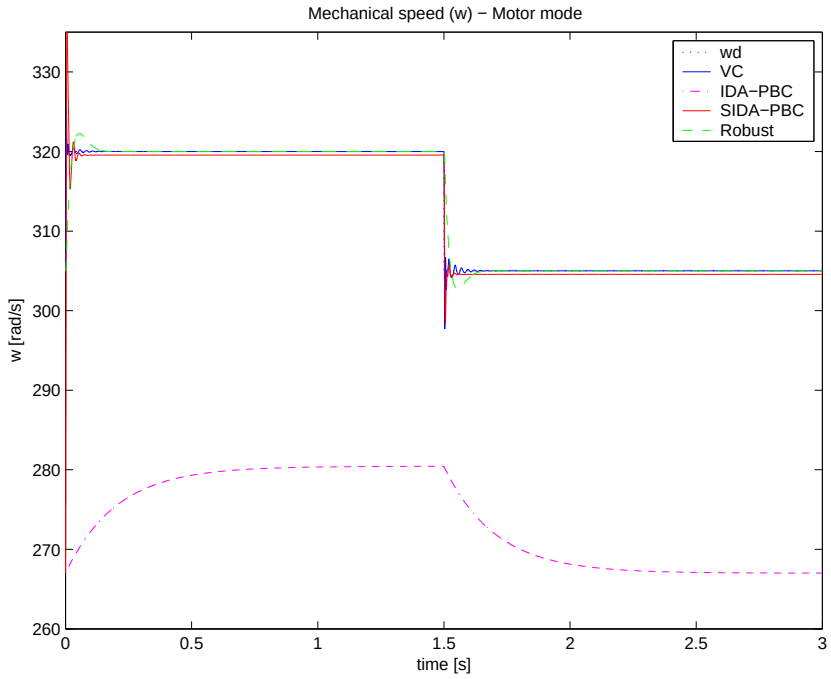

Figure 4.24: Simulation results, comparison: mechanical speed ω under uncertain parameters.

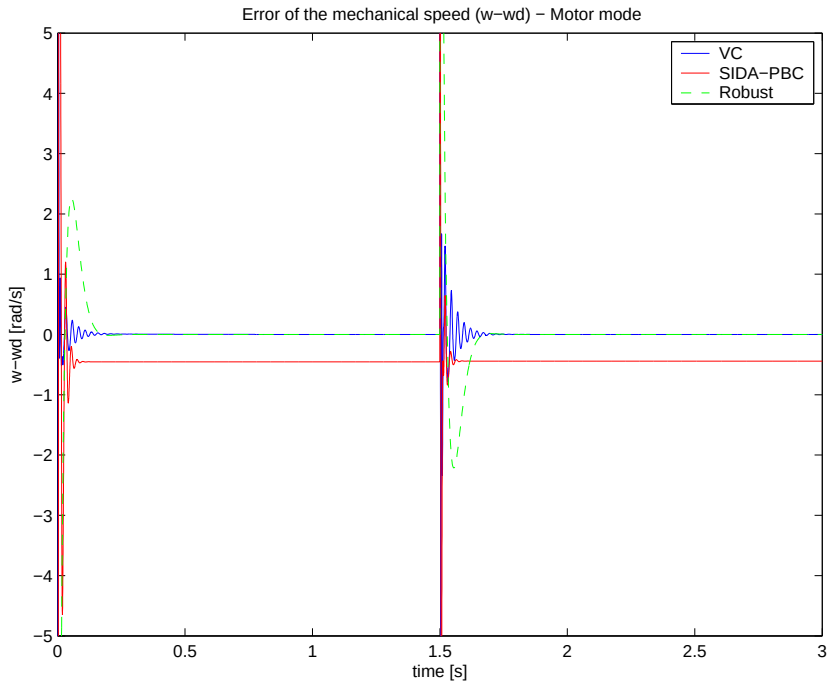

Figure 4.25: Simulation results, comparison: error of the mechanical speed $\omega - \omega_d$ under uncertain parameters.

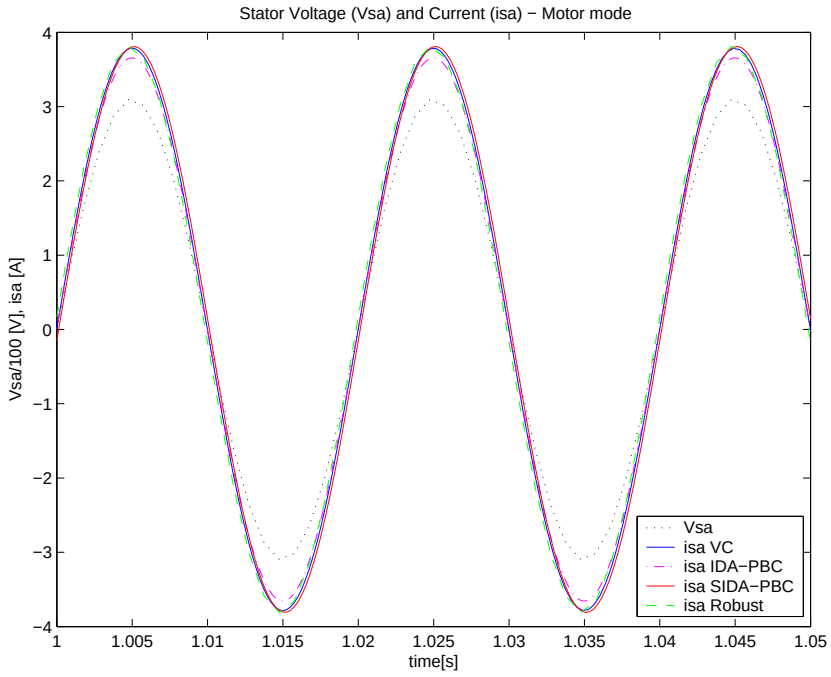

Figure 4.26: Simulation results, comparison: A-stator voltage and current (V_{sa}, i_{sa}) under uncertain parameters.

  - *Cons*: No global stability proved, estimation of the stator flux required, stator power is expressed in rotor current terms.

- **IDA-PBC**

  - *Pros*: Stability proved using cascaded properties and all control variables are directly measured.
  - *Cons*: No robustness and slow mechanical transient response.

- **SIDA-PBC**

  - *Pros*: Stability proved with a global Lyapunov function, fast transient response to the mechanical variables, and all the control variables are measurable.
  - *Cons*: No robustness.

- **Robust IDA-PBC**

  - *Pros*: Stability proved for the electrical part, fast transient response to the mechanical variables and all the control variables are measurable.
  - *Cons*: No stability proved for the outer-loop.

For all these reasons, the controller that is chosen in this thesis for the experimental implementation is the one we have called "Robust".

4.2 Control of the back-to-back converter

In this section an IDA-PBC controller for the back-to-back converter is presented. As explained in Section 1.3, the B2B is made of a full-bridge rectifier (which controls the DC link voltage) and a three-phase inverter (which generates a PWM voltage to feed the DFIM rotor side). For control purposes, only the rectifier subsystem is considered, while the inverter acts as an static interconnection with a load or current source. Notice that the DFIM can act also as a current source depending on the operation state.

An important requirement is the ability to handle a bidirectional power flow, due that power can flow in both directions through the back-to-back (rectifier+inversor) converter connected to the DFIM rotor. Since the aim of the control scheme is to keep the intermediate DC-bus to a constant voltage, the rectifier's load current can have any sign (although it can be supposed to be, approximately, piecewise-constant in time).

Traditional control strategies establish two loops in a cascade structure: a line current inner loop for power factor compensation and an output voltage outer loop for voltage regulation. Then the control of each loop can be done linearizing around an operation point with PI controllers, or using feedback linearization [53], or Sliding Mode Control [43][59].

A simple zero dynamics study shows that, depending on the power flow direction, the power converter could be unstable for certain outputs. This fact advises against the use of the typical variables as outputs (inductor current and capacitor voltage) and requires a different control method to avoid instability for a bidirectional use of the power converter. It should be noticed that standard output regulation procedures to solve the bidirectional

case cannot be applied, since, no matter which output is chosen (for example in a boost converter, either capacitor voltage or inductor current) the zero dynamics is unstable for one of the two modes of operation (see also [81]).

To avoid this problem passive techniques can be applied to design a controller able to operate in both cases. In particular, the IDA-PBC methodology was used in [39], or an adaptive scheme proposed in [33].

This Section presents a zero dynamics study of a DC-DC boost converter in order to investigate the stability for both power flow directions. This simpler power converter is studied instead of the full-bridge rectifier because the assumption of a sinusoidal voltage source implies the discussion of a class A, 2nd type, Abel ODE, which has no explicit analytical solution.

After this discussion, applying the IDA-PBC technique and a GSSA model (see Section 2.4), a control law for a full-bridge rectifier is obtained and simulated.

4.2.1 Zero dynamics of a full-bridge rectifier

The full-bridge rectifier has been presented in subsection 1.3.1. The averaged model of the power converter is described by

$$\begin{aligned} L\frac{\mathrm{d}i}{\mathrm{d}t} &= -Sv_{DC} - ri + v_i \\ C\frac{\mathrm{d}v_{DC}}{\mathrm{d}t} &= Si - i_{DC} \end{aligned}$$

where now S takes values in a continuum set $S \in [-1, 1]$. As said before v_i is an AC voltage source and the system can be rewritten as

$$\begin{aligned} L\frac{\mathrm{d}i}{\mathrm{d}t} &= -S(t)v_{DC}(t) - ri(t) + E\sin(\omega_s t) \\ C\frac{\mathrm{d}v_{DC}}{\mathrm{d}t} &= S(t)i(t) - i_{DC} \end{aligned} \tag{4.37}$$

where E is the amplitude of the AC voltage and ω_s is its frequency (typically the grid frequency).

Notice that i_{DC} is considered constant, but to achieve bidirectionality no assumption is made on its sign, *i.e.* $i_l \in \mathbb{R}$. Notice that i_{DC} is considered constant, but in order to get a bidirectional power flow no assumption is made on its sign, *i.e.* $i_l \in \mathbb{R}$. The zero dynamics studies the behaviour of the internal variables assuming that the control objective is achieved. We will first study the zero dynamics taking the inductor current i as output and after that the zero dynamics when the control goal is the the capacitor voltage V.

Current-output Analysis

As mentioned before, the inductor current control specification is

$$i(t) = I_d \sin(\omega_s t) \tag{4.38}$$

for an appropriate I_d. Replacing (4.38) into the dynamical equations (4.37) we obtain the control law, $S = u(t)$

$$u(t) = \frac{(E - rI_d)\sin(\omega_s t) - \omega_s L I_d \cos(\omega_s t)}{v_{DC}(t)}$$

and the remaining dynamics of the dc bus voltage

$$\frac{\mathrm{d}V}{\mathrm{d}t} = \frac{(E - rI_d)I_d \sin^2(\omega_s t) - \omega_s L I_d^2 \sin(\omega_s t)\cos(\omega_s t) - v_{DC}(t) i_{DC}}{C v_{DC}(t)}. \tag{4.39}$$

The zero dynamics is the solution of the previous differential equation (4.39), which can be written in a simple form as

$$\frac{\mathrm{d}V}{\mathrm{d}t} = -\frac{1}{C} i_{DC} + \frac{g(t)}{v_{DC}},$$

where g is a function on time. This equation is a class A, 2nd type, Abel ODE, for which numerical simulations show the existence of unstable solutions when $i_{DC} < 0$; Abel equations are known to appear in tracking problems for power converters [35]. Notice that this differs from the case with a resistive load [43], $i_{DC} = i_{DC}(t) = \frac{v_{DC}(t)}{R}$, for which the solution is a stable Bernoulli ODE.

Voltage-output Analysis

Now we set $v_{DC} = v_{DC}^d$ and, using (4.37), the control law is obtained as

$$u(t) = \frac{i_{DC}}{i(t)}.$$

The remaining equation for the inductor current is then

$$\frac{\mathrm{d}i}{\mathrm{d}t} = \frac{-ri(t)^2 + i(t)E\sin(\omega_s t) - i_{DC} v_{DC}^d}{L i(t)}.$$

This equation is, again, a class A, 2nd type, Abel ODE and, again, numerical simulations show the instability of their solutions, but now for $i_{DC} > 0$.

4.2.2 Zero dynamics of a boost converter

In order to better understand the unstable behaviour of the full-bridge rectifier, we study a similar but simpler converter, namely the dc-dc boost shown in Figure 4.27, for which the control goal is to regulate V to a desired value V_d, taking E as a constant input voltage.

The dynamical equations of the dc-dc boost converter are

$$\begin{aligned} L\frac{\mathrm{d}i}{\mathrm{d}t} &= -ri - uV + E \\ C\frac{\mathrm{d}V}{\mathrm{d}t} &= ui - i_l \end{aligned} \tag{4.40}$$

where i is the inductor current, V the capacitor voltage, $L > 0$ is the inductance, $C > 0$ is the capacitance, $r > 0$ describes the inductor losses, $E > 0$ is the input voltage, i_l is the load port current (notice that if the port is connected to a dissipative load one has $i_l > 0$ and if it is connected to a source $i_l < 0$) and u is the control action.

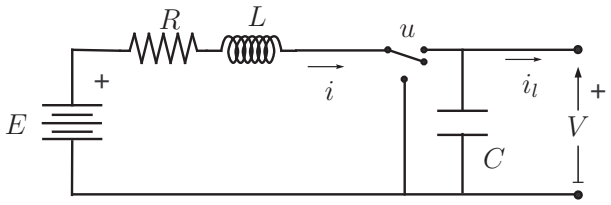

Figure 4.27: DC-DC boost power converter.

Voltage-output Analysis

The main goal of the dc-dc boost is to regulate the V voltage to a desired value V_d. The zero-dynamics gives the system behavior when the control objective is achieved. From (4.40), the equilibrium points for a desired output $V = V_d$ correspond to current values given by

$$i^* = \frac{E \pm \sqrt{E^2 - 4rV_d i_l}}{2r},$$

where

$$E^2 - 4rV_d i_l > 0$$

is assumed. From (4.40), with $V = V_d$ and $\dot{V} = 0$, the current dynamics is

$$\frac{\mathrm{d}i}{\mathrm{d}t} = \frac{-ri^2 + iE + i_l V_d}{Li}.$$

This dynamics will be (linearly) stable as long as the partial derivative of the right-hand side with respect to i evaluated at i^* is negative; thus, the stability depends on the value of the equilibrium point i^* and of i_l. Figure 4.28 describes the stability of several equilibrium points, depending on the values of i_l and i^*. We can observe that for a $i_l > 0$ one of the two equilibrium points is unstable (this fact recovers the results given in [81]), and furthermore this equilibrium point turns out to be the most suitable because it corresponds to the smallest inductor current i. On the other hand, for $i_l < 0$ both equilibrium points are stable.

Current-output Analysis

For an output-current analysis, the zero-dynamics is obtained by setting $i = i^*$ and $\frac{\mathrm{d}i}{\mathrm{d}t} = 0$. The remaining dynamics is

$$\frac{\mathrm{d}V}{\mathrm{d}t} = \frac{V_d i_l}{CV} - \frac{i_l}{C}.$$

Computing the derivative of the right-hand side with respect to V at $V = V_d$ yields

$$-\frac{i_l}{V_d C},$$

and hence the equilibrium point is stable (unstable) if $i_l > 0$ ($i_l < 0$); see Figure 4.29.

The obtained results are similar to those in [81], but here we have extended the study to a bidirectional power flow. Summing up, for the dc-dc boost converter no single output yields a stable zero dynamics for power flowing both ways. This analysis lends weight to the hypothesis that a similar result holds for the more complex full-bridge rectifier, and this is confirmed by numerical simulations.

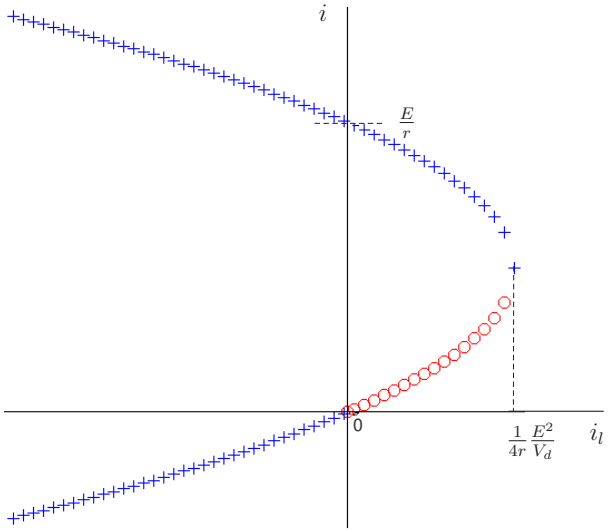

Figure 4.28: Stability of the equilibrium points for $V = V_d$. (+) stable and (∘) unstable points.

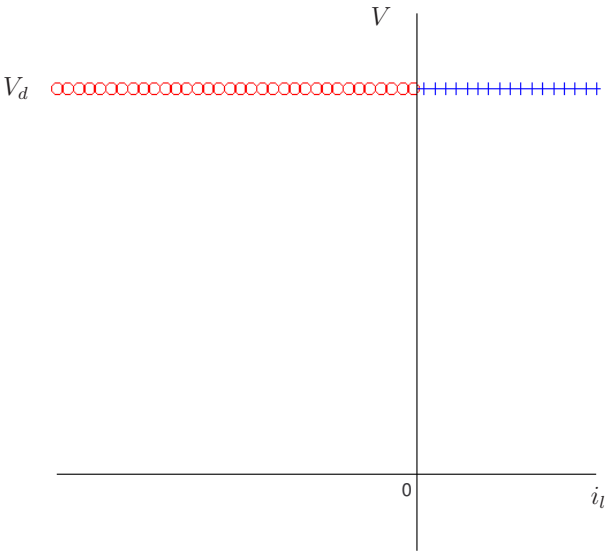

Figure 4.29: Stability of the equilibrium points for $i = i^*$. (+) stable and (∘) unstable points.

4.2.3 IDA-PBC for an ac-dc boost rectifier

Since for a single phase system the dq-transformation can not be applied we use the GSSA theory. Form the control model obtained in Section 2.4 an IDA-PBC controller is designed. Let us remind the control objectives,

- the DC value of v_{DC} voltage should be equal to a desired constant v_{DC}^d, and
- the power factor of the converter should be equal to one. This means that the inductor current should be $i = LI_d \sin(\omega_s t)$, where I_d is an appropriate value to achieve the first objective via energy balance.

As discussed in the previous Chapter, this model differs from [39] in the $-i_{DC}\sqrt{2x_1}$ term, that now is included in the g matrix. This change is instrumental in achieving a bidirectional power flow capability, since in [39] $i_{DC}\sqrt{2x_1}$ was included in the dissipation matrix, for which $i_{DC} \geq 0$ was necessary.

The control objectives for the rectifier are a DC value of the output voltage, $v_{DC} = \frac{1}{C}q$, equal to a desired point, v_{DC}^d, which in GSSA variables translates to

$$x_1^* = \frac{1}{2}C^2(v_{DC}^d)^2,$$

and a power factor on the AC side equal to one, which in our truncated GSSA variables can be expressed as $x_2^* = 0$. To obtain the x_3^* equilibrium point, we compute the derivative of the Hamiltonian function (2.35),

$$\dot{H} = \frac{1}{C}\dot{x}_1 + \frac{2}{L}\dot{x}_2 x_2 + \frac{2}{L}\dot{x}_3 x_3,$$

which, using the dynamical equations (2.34), is

$$\dot{H} = -\frac{1}{C}i_{DC}\sqrt{2x_1} + \frac{2}{L}\dot{x}_2 x_2 + \frac{2}{L}\dot{x}_3 x_3, \tag{4.41}$$

In the equilibrium point $\dot{H} = 0$, and taking into account that $x_2^* = 0$ and $\frac{\sqrt{2x_1^*}}{C} = v_{DC}^d$,

$$x_3^* = \frac{-\frac{EL}{2r} + \sqrt{\left(\frac{EL}{2r}\right)^2 - \frac{2L^2}{r}i_{DC}v_{DC}^d}}{2},$$

where we have chosen for x_3^* the solution with the smallest magnitude.

The central idea of Interconnection and Damping Assignment-Passivity Based Control (IDA-PBC) [66] is to assign to the closed-loop a desired energy function via the modification of the interconnection and dissipation matrices. The desired target dynamics is a Hamiltonian system of the form

$$\dot{x} = (J_d - R_d)(\partial H_d)^T$$

where $H_d(x)$ is the new total energy and $J_d = -J_d^T$, $R_d = R_d^T \geq 0$, are the new interconnection and damping matrices, respectively. To achieve stabilization of the desired equilibrium point we impose $x^* = \arg\min H_d(x)$. The matching objective is achieved if and only if the following PDE

$$(J - R)(\partial H)^T + g = (J_d - R_d)(\partial H_d)^T \tag{4.42}$$

is satisfied, where $H_d(x) = H(x) + H_a(x)$, $J_d = J + J_a$, $R_d = R + R_a$, and we have redefined $g = g_1(x_1) i_{DC} + g_2 E$, where $g_1(x_1) = (-\sqrt{2x_1}, 0, 0)^T$ and $g_2 = (0, 0, -1/2)^T$.

Fixing the interconnection and damping matrices as $J_d = J$ and $R_d = R$, equation (4.42) simplifies to

$$-(J - R)(\partial H_a)^T + g = 0,$$

and, defining $k(x) = (k_1, k_2, k_3)^T = (\partial H_a)^T$, one gets

$$\begin{aligned} 0 &= u_1 k_2 + u_2 k_3 - i_{DC}\sqrt{2x_1} && (4.43)\\ 0 &= -u_1 k_1 + \frac{r}{2} k_2 - \frac{\omega_s L}{2} k_3 && (4.44)\\ 0 &= -u_2 k_1 + \frac{\omega_s L}{2} k_2 + \frac{r}{2} k_3 - \frac{E}{2}. && (4.45) \end{aligned}$$

Equations (4.44) and (4.45) can be solved for the controls,

$$\begin{aligned} u_1 &= \frac{r k_2 - \omega_s L k_3}{2k_1} && (4.46)\\ u_2 &= \frac{\omega_s L k_2 + r k_3 - E}{2k_1}, && (4.47) \end{aligned}$$

and replacing (4.46) and (4.47) in (4.43) the following PDE is obtained:

$$r(k_2^2 + k_3^2) - E k_3 - 2 i_{DC}\sqrt{2x_1} k_1 = 0. \tag{4.48}$$

If one is interested in control inputs u_1 and u_2 which only depend on x_1, one can take $k_1 = k_1(x_1)$, $k_2 = k_2(x_1)$ and $k_3 = k_3(x_1)$, and consequently, using the integrability condition

$$\frac{\partial k_i}{\partial x_j}(x) = \frac{\partial k_j}{\partial x_i}(x)$$

one gets that $k_2 = a_2$ and $k_3 = a_3$ are constants. Then, from (4.48),

$$k_1 = \frac{1}{2 i_{DC}\sqrt{2x_1}} \left(r\left(a_2^2 + a_3^2\right) - E a_3 \right). \tag{4.49}$$

The equilibrium condition

$$\partial H_d|_{x=x^*} = (\partial H + \partial H_a)|_{x=x^*} = 0$$

is

$$\begin{aligned} \frac{1}{C} + k_1(x_1^*) &= 0 && (4.50)\\ \frac{2}{L} x_2^* + a_2 &= 0\\ \frac{2}{L} x_3^* + a_3 &= 0 \end{aligned}$$

and, since $x_2^* = 0$, one obtains $a_2 = 0$ and $a_3 = -\frac{2}{L} x_3^*$. Substituting these values of a_2 and a_3 in (4.49) yields

$$k_1 = -\frac{1}{C}\sqrt{\frac{x_1^*}{x_1}}$$

which satisfies the equilibrium condition (4.50). One can now solve the PDE (4.48) and find H_a

$$H_a = -\frac{2\sqrt{x_1^*}}{C}\sqrt{x_1} - \frac{2}{L}x_3^* x_3,$$

from which

$$H_d = \frac{1}{C}x_1 + \frac{1}{L}x_2^2 + \frac{1}{L}x_3^2 - \frac{2\sqrt{x_1^*}}{C}\sqrt{x_1} - \frac{2}{L}x_3^* x_3. \tag{4.51}$$

In order to guarantee that H_d has a minimum at $x = x^*$, the Hessian of H_d has to obey

$$\left.\frac{\partial^2 H_d}{\partial x^2}\right|_{x=x^*} > 0.$$

From (4.51)

$$\left.\frac{\partial^2 H_d}{\partial x^2}\right|_{x=x^*} = \begin{bmatrix} \frac{1}{2C\sqrt{x_1^*}} & 0 & 0 \\ 0 & \frac{2}{L} & 0 \\ 0 & 0 & \frac{2}{L} \end{bmatrix},$$

which is always positive definite, so the minimum condition is satisfied. Substituting everything in (4.46), (4.47), and taking into account that the equation satisfied by x_3^* can be written as

$$\frac{2r}{L}x_3^* + E = -\frac{L}{x_3^*}i_{DC}v_{DC},$$

the control law can be expressed in terms of the output voltage v_{DC} as

$$u_1 = -\frac{\omega_s C x_3^* v_{DC}}{v_{DC}^d} \tag{4.52}$$

$$u_2 = -\frac{CLi_{DC}v_{DC}}{2x_3^*}. \tag{4.53}$$

Writing (4.52) and (4.53) in real coordinates, using the inverse GSSA transformation

$$v = 2\left(u_1\cos(\omega_s t) - u_2\sin(\omega_s t)\right),$$

and taking into account that $v = -S\sqrt{2x_1}$, the control action simplifies finally to

$$S = \frac{2\omega_s x_3^*}{v_{DC}^d}\cos(\omega_s t) - \frac{Li_{DC}}{x_3^*}\sin(\omega_s t).$$

Simulations

In this section we implement a numerical simulation of the IDA-PBC controller for a full-bridge rectifier. We use the following parameters: $r = 0.1\Omega$, $L = 1$mH, $C = 4500\mu$F, $\omega_s = 2\pi 50$rad s^{-1} and $E = 68.16$V. The desired voltage is fixed at $v_{DC}^d = 150$V, and the load current varies from $i_{DC} = -1$A to $i_{DC} = 3$A at $t = 1$s. Figure 4.30 shows the bus voltage v_{DC}. It starts at $v_{DC} = 140$V and then goes to the desired value, for different load current values. The small static error corresponds to the non-considered harmonics in the control design using GSSA. AC voltage and current are depicted in Figure 4.31. Notice that when $i_{DC} > 0$ (for $t < 1$), current i is in phase with voltage v_i and power flows to the load; when $i_{DC} < 0$ (for $t > 1$), i is in opposite phase with v_i and power flows *from* the load to the AC main. Finally, Figure 4.32 shows that the control action S remains in $[-1, 1]$, which allows its discrete experimental implementation using a PWM scheme.

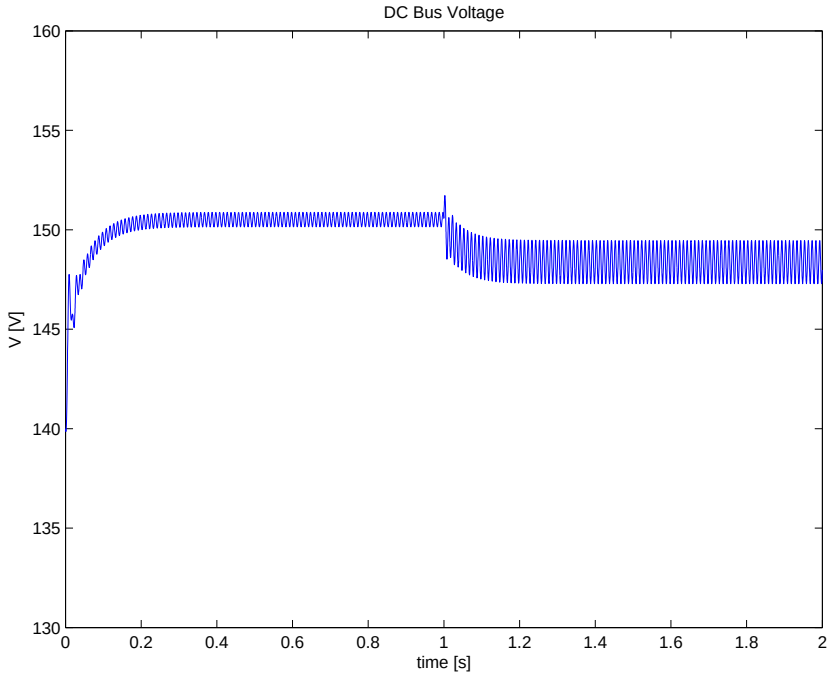

Figure 4.30: Simulation results: bus voltage v_{DC} waveform.

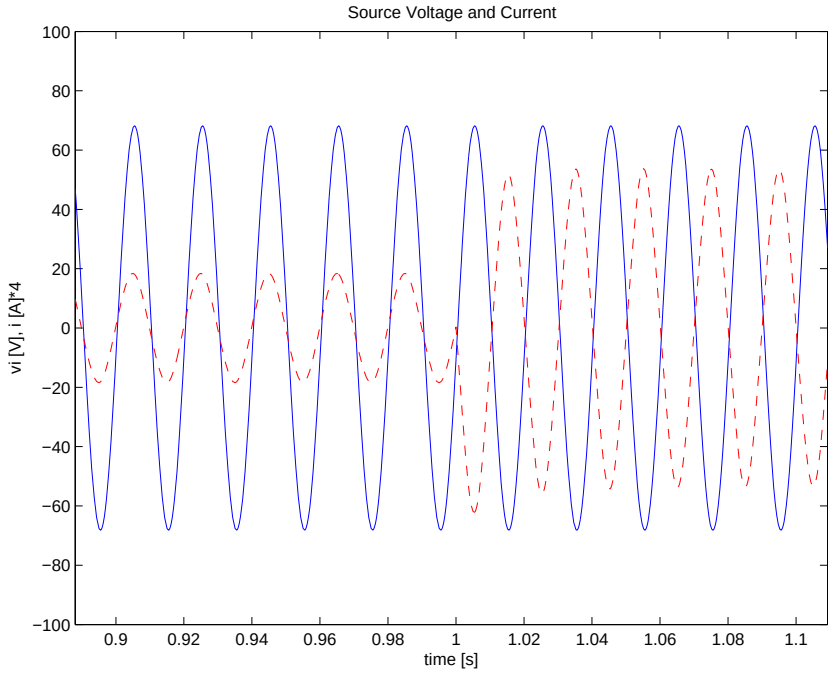

Figure 4.31: Simulation results: source voltage v_i and current i waveforms, showing the change in power flow.

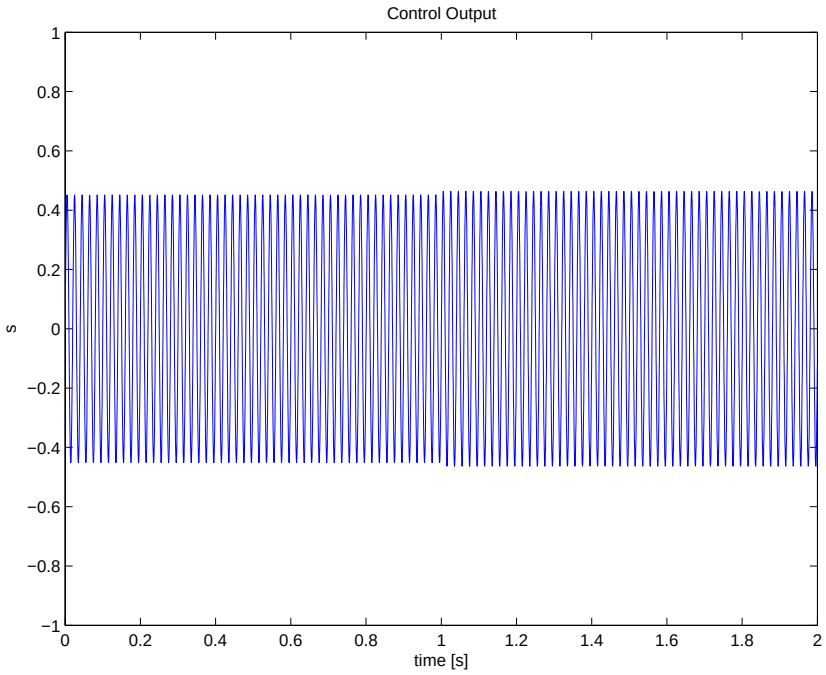

Figure 4.32: Simulation results: control action S remains in $[-1, 1]$.

4.3 Control of the Flywheel Energy Storage System

In this Section some simulations of the Flywheel Energy Storage System are presented, using the controllers designed for the DFIM and the B2B. In particular, the DFIM is controlled by the so-called robust IDA-PBC method, with the outer-loop and the integral term designed in subsection 4.1.4. The complete system is simulated in order to check whether the policy management described in Section 1.4 is achieved.

Table 4.2 shows the parameter values used in this simulation. A three-phase network is considered (effective voltage $V_f = 380$V and frequency $f = 50$Hz or $\omega_s = 2\pi 50$). The maximal power delivered by the network is set to $P_n^{MAX} = 2000$W, and the load is connected at $t = 1$s and disconnected at $t = 2$s.

	Parameters (in SI units)
DFIM	$L_{sr} = 0.71$, $L_s = 0.725$, $L_r = 0.715$, $R_s = 4.92$, $R_r = 4.42$ $J_m = 0.11512$, $B_r = 0.005$
B2B	$r = 0.5$, $L = 0.001$, $C = 0.0045$, $v_i = 68.16\sin(\omega_s t)$
Local Load	$R_{load} = 50$, $L_{load} = 0.005$

Table 4.2: Simulation parameter values (in SI units) for the DFIM coupled to a flywheel and the B2B.

Figures 4.33 and 4.34 show the evolution of the relevant output quantities of the system. The active power delivered by the network is kept under its maximal value even when the power required by the local load is higher, Figure 4.33. Notice that, at the same time, the

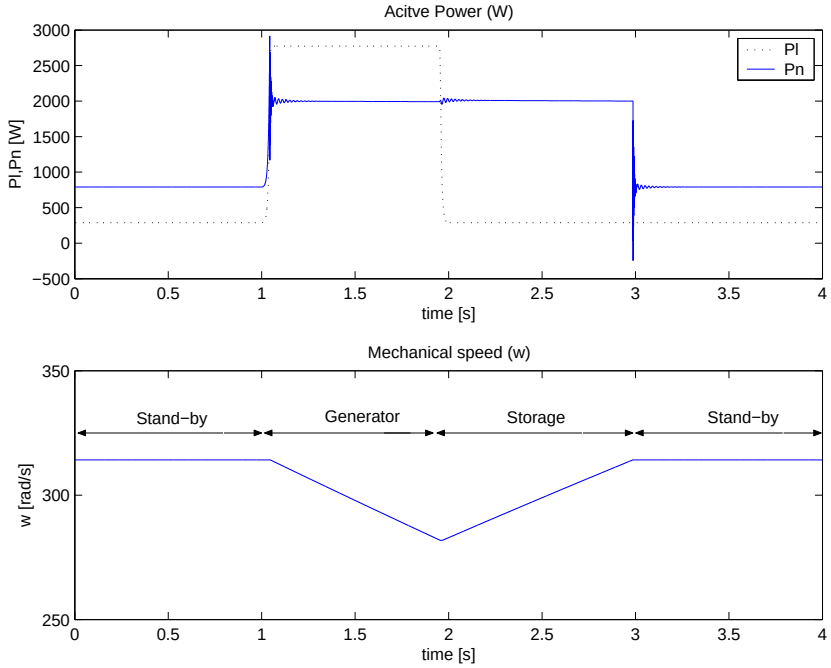

Figure 4.33: Simulation results: Network and load active powers (P_n and P_l), and mechanical speed ω.

mechanical speed decreases (we are in the so-called *generator* mode). When the load is disconnected (at $t = 2$s), the system keeps the maximal active power to accelerate the flywheel, until it reaches the optimum speed (*storage* mode). Finally, the system acts as a motor to keep the system at its optimal speed (*stand-by* mode). Figure 4.34 shows the reactive power compensation. Notice that the a-phase network voltage (V_{na}) and current (i_{na}) are in phase even if the load current (i_{la}) is advanced in phase. Notice that neither *generator* nor *storage* modes arrive to their respective fixed points; these modes work always in the transient regime. In fact, the equilibrium points of both modes could be very *undesirable* (the mechanical speed becomes negative for the generator mode or very high for the storage one, for typical values of the system parameters and requirements). This problem , with a complex mathematical description [29], can be solved computing the energy balance and estimating the flywheel speed in function of the local load, the connection time and the maximal power network.

Figure 4.35 shows the behavior of the DC-bus voltage V during this sequence of changes. Its value remains close to the desired value $V^d = 150$V. A small oscillation corresponding to a second harmonic component of the grid frequency ω_s appears due the dynamics of the rectifier [43]. Notice that in the generator and storage modes the ripple amplitude changes. This can be associated to the transient behavior of the modes and to the fact that the oscillations are a function of the load current (the rotor currents in this case). As was computed in Section 1.4, the rotor currents increase with the difference between the optimal and the mechanical speed, so this ripple also increases. In any case, when the DFIM is at steady-state (stand-by mode) the bus voltage remains at the desired value.

The remaining control goal for the rectifier is to allow a bidirectional power flow with a high power factor. Figure 4.36, displaying the AC-source voltage v_i and the current i of

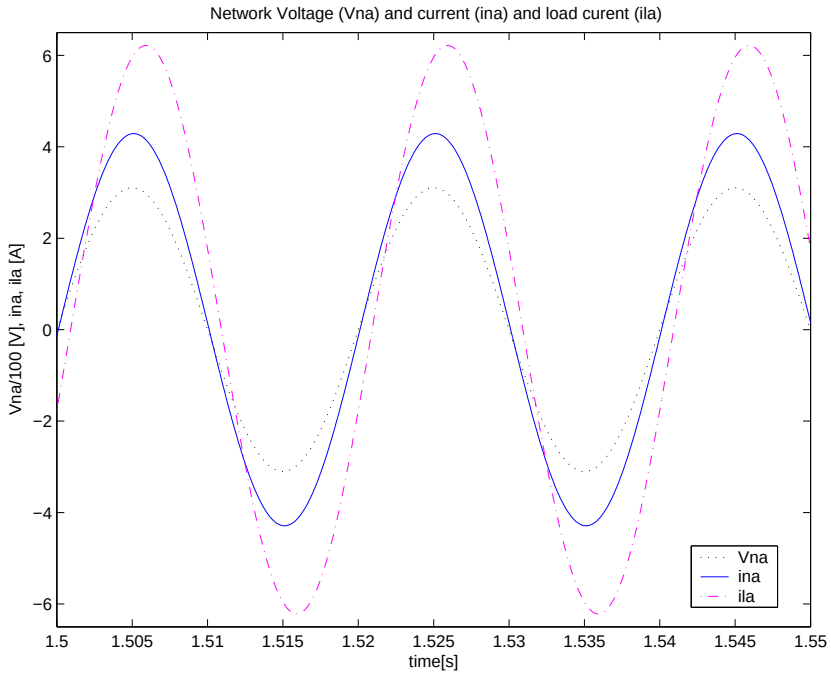

Figure 4.34: Simulation results: A-network voltage and current (V_{na} and i_{na}) and A-load current i_{la}.

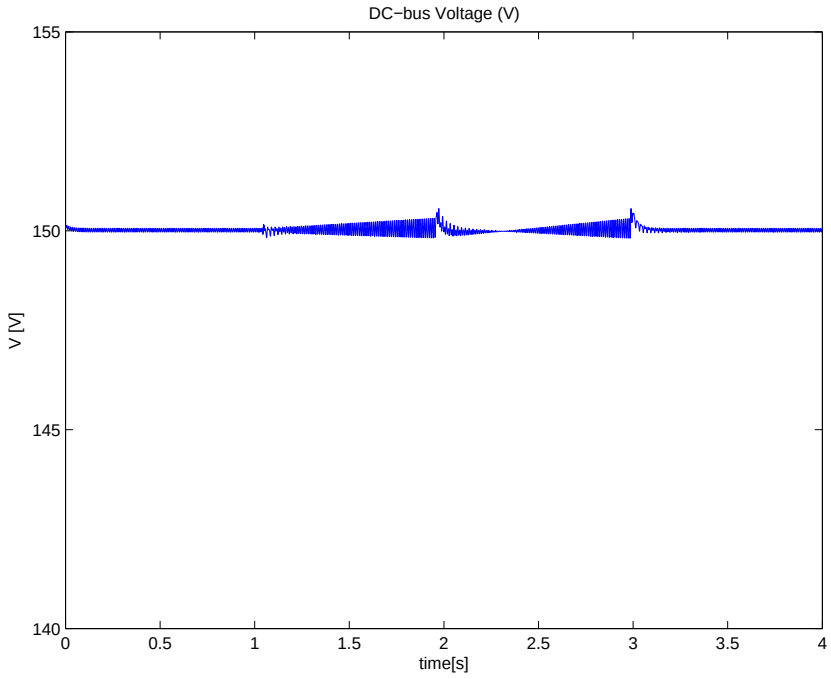

Figure 4.35: Simulation results: DC-bus voltage V.

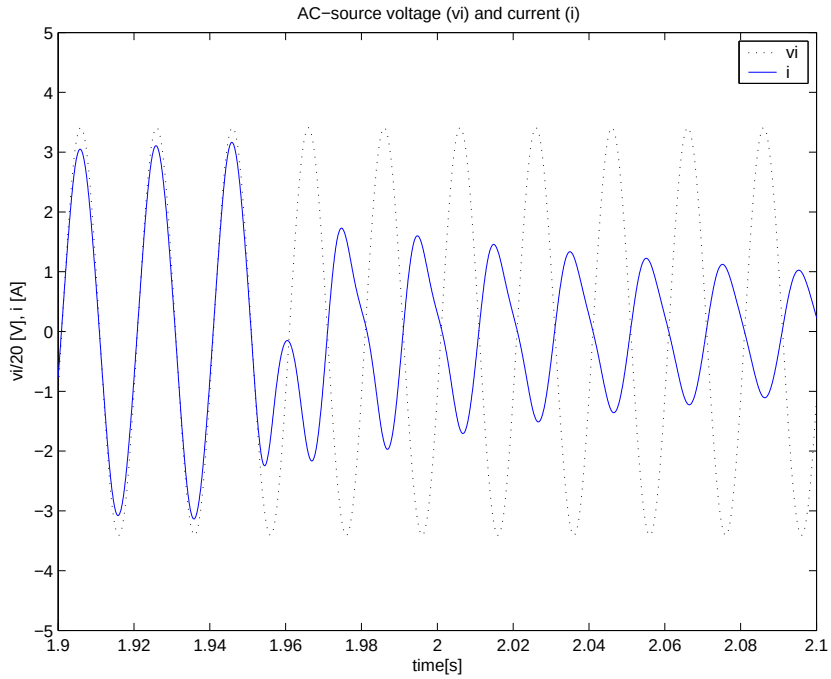

Figure 4.36: Simulation results: AC-source voltage v_i and current i.

the rectifier, shows that the objective is achieved.